The researches of medical and environmental radiation protection dose

Abstract

Nowadays, with the development of modern radiation science, application of radiation exposure has been paid more and more attention in various fields. Although there are many benefits for human by the use of radiation in such as medical diagnose and treatment, utilization of nuclear power, more efforts should be made to radiation hazards and their control that are often neglected. The researches in this study were intended to meet the requirements with the center of radiation protection dose in a wide range which attracts the most attention and are involved, either directly or indirectly, with ionizing radiation, including diagnostic exposure doses in paediatric CT, radiation doses in normal tissues which surrounding the targets in radiotherapy, and environmental exposure doses in Fukushima nuclear accidental areas.

In the researches about paediatric CT, the reference radiation dose and organ doses from chest CT studies of children were estimated by using the data of clinical practice of the National Center for Child Health and Development in Japan. In composing local diagnostic reference doses and organ doses, the aim of this research was to provide a reliable and accurate data on the exposures in X-ray CT examinations for paediatric patients, which could be useful for optimization of radiation protection. Moreover, to evaluate the changes of organ doses depending on the thickness of the soft tissue on body surface in paediatric abdomen CT, radiation doses were measured with radiophotoluminescence glass dosemeters set in various organ positions within a 6-year-old child anthropomorphic phantom with slices of soft tissue equivalent materials attached on the surface, and organ doses were evaluated from the measurement values.

In the researches of radiation treatment, the characteristics of the hepatic tumor movement caused by respiration were evaluated by using fluoroscopy. To decrease exposure doses in healthy organs that surrounding targets in tumor tracking treatment, the feasibility of prospective tracking of respiratory caused tumor motion signal based on autoregressive model was also tested to compensate the retardation time that often exists between the acquisition of motion signal and the action execution.

In the researches of environmental radiation exposure in Fukushima nuclear

accidental areas, radiocesium contaminated soil was obtained from a polluted area in Fukushima and was remedied under strict control by use of electrokinetics, and to accurately measure surface radiation doses after depollution operations, a shield for environmental radiation dose survey meters in badly contaminated areas has been developed.

According to the results of the researches, a set of CTDIs and organ doses in paediatric chest CT scan was compiled for the National Center for Child Health and Development based on children's weights. Organ doses in paediatric abdomen CT were evaluated under different thicknesses of soft tissue on the surface of the same child anthropomorphic phantom. In the radiation therapy, thoracic and abdominal tumor motion has been verified to be pace with respiratory movement, and Burg's method has been proved to be effective to predict tumor motion in real-time, and moreover, it could make a contribution to protection for normal organs. Radiocesium contaminated soil was laboratory depolluted effectively by use of electrokinetic remediation technology, and a new shield for survey meters was successfully developed to precisely measure the environmental radiation dose and evaluate decontamination work in the Fukushima.

Contents

Section Ⅱ   Protection in Paediatric CT

Section Ⅲ   Protection in Radiotherapy

Section Ⅳ　Protection in Environment

Section Ⅰ   Basic Information

In this section, some basic information about radiation and radiation protection is going to be introduced, and it will start the first step of our whole research.

Chapter 1 Introduction to Radiation

1.1 Overview

Radiation is energy in the form of waves or streams of particles. There are many kinds of radiation all around us. When people hear the word radiation, they often think of atomic energy, nuclear power and radioactivity, but radiation has many other forms. Sound and visible light are familiar forms of radiation; other types include ultraviolet radiation (that produces a suntan), infrared radiation (a form of heat energy), and radio and television signals.

Uncontrolled man-made and natural radiation carries a potential risk to the health and safety of workers and the public. The purpose of this chapter is to provide clear and simple information about radiation: what it is, where it comes from and how it is used. It also presents information on radiation types and radiation doses.

1.2 Atoms and Isotopes
1.2.1   Atoms: Where all matter begins

Atoms form the basic building blocks of all matter. In other words, all matter in the world begins with atoms – they are elements like oxygen, hydrogen, and carbon. An atom consists of a nucleus – made up of protons and neutrons that are kept together by nuclear forces and electrons that are in orbit around the nucleus.

Each element is distinguished by the number of protons in its nucleus. This number, which is unique to each element, is called the "atomic number". In an atom of neutral charge, the atomic number is also equal to the number of electrons. An atom's chemical properties are determined by the number of electrons, which is normally equal to the atomic number. Atoms from one or more elements combine to form molecules. A nuclide is a specific type of atom characterized by the number of protons and neutrons in its nucleus, which approximates the mass of the nuclide. The number that is sometimes given with the name of the nuclide is called its mass number (the total number of protons and neutrons in the nucleus).

1.2.2   Isotopes

An isotope is a variant of a particular chemical element. While all isotopes of a given element have the same number of protons, each isotope has a different number of neutrons.

For example, hydrogen has three isotopes (or variants):

- hydrogen-1 (contains one proton and no neutrons)
- hydrogen-2, which is called deuterium (contains one proton and one neutron)
- hydrogen-3, which is called tritium (contains one proton and two neutrons)

An isotope is stable when it has a balanced number of neutrons and protons. In general, when an isotope is small and stable, it contains close to an equal number of protons and neutrons. Isotopes that are larger and stable have slightly more neutrons than protons

1.2.3 Radioisotopes

Isotopes that are not stable and emit radiation are called radioisotopes. A radioisotope is an isotope of an element that undergoes spontaneous decay and emits radiation as it decays. During the decay process, it becomes less radioactive over time, eventually becoming stable. Once an atom reaches a stable configuration, it no longer gives off radiation. For this reason, radioactive sources − or sources that spontaneously emit energy in the form of ionizing radiation as a result of the decay of an unstable atom − become weaker with time.

The time it takes for a radioisotope to decay to half of its starting activity is called the radiological half-life, which is denoted by the symbol t½. Each radioisotope has a unique half-life, and it can range from a fraction of a second to billions of years. For example, iodine-131 has an eight-day half-life, whereas plutonium-239 has a half-life of 24,000 years. A radioisotope with a short half-life is more radioactive than a radioisotope with a long half-life, and therefore will give off more radiation during a given time period.

There are three main types of radioactive decay:
- Alpha decay: Alpha decay occurs when the atom ejects a particle from the nucleus, which consists of two neutrons and two protons. When this happens, the atomic number decreases by 2 and the mass decreases by 4.
- Beta decay: In basic beta decay, a neutron is turned into a proton and an electron is emitted from the nucleus. The atomic number increases by one, but the mass only decreases slightly.
- Gamma decay: Gamma decay takes place when there is residual energy in the nucleus following alpha or beta decay, or after neutron capture (a type of nuclear reaction) in a nuclear reactor. The residual energy is released as a photon of gamma radiation. Gamma decay generally does not affect the mass or atomic number of a radioisotope.

The number of nuclear disintegrations in a radioactive material per unit time is called

the activity. The activity is used as a measure of the amount of a radionuclide, and it is measured in becquerel (Bq). 1 Bq = 1 disintegration per second.

If the original source of the radioactivity is known, it can be predicted how long it will take to decay to a given activity. The decay is exponential and the isotope must go through many half-lives to become nonradioactive.

1.3 Types and Sources of Radiation

Radiation is energy in the form of waves of particles. There are two forms of radiation – non-ionizing and ionizing

1.3.1 Non-ionizing radiation

Non-ionizing radiation has less energy than ionizing radiation; it does not possess enough energy to produce ions. Examples of non-ionizing radiation are visible light, infrared, radio waves, microwaves, and sunlight.

Global positioning systems, cellular telephones, television stations, FM and AM radio, baby monitors, cordless phones, garage-door openers, and ham radios use non-ionizing radiation. Other forms include the earth's magnetic field, as well as magnetic field exposure from proximity to transmission lines, household wiring and electric appliances. These are defined as extremely low-frequency (ELF) waves and are not considered to pose a health risk.

1.3.2 Ionizing radiation

Ionizing radiation is capable of knocking electrons out of their orbits around atoms, upsetting the electron/proton balance and giving the atom a positive charge. Electrically charged molecules and atoms are called ions. Ionizing radiation includes the radiation that comes from both natural and man-made radioactive materials.

There are several types of ionizing radiation:

Alpha radiation (α)

Alpha radiation consists of alpha particles that are made up of two protons and two neutrons each and that carry a double positive charge. Due to their relatively large mass and charge, they have an extremely limited ability to penetrate matter. Alpha radiation can be stopped by a piece of paper or the dead outer layer of the skin. Consequently, alpha radiation from nuclear substances outside the body does not present a radiation hazard. However, when alpha-radiation-emitting nuclear substances are taken into the body (for example, by breathing them in or by ingesting them), the energy of the alpha radiation is completely absorbed into bodily tissues.

For this reason, alpha radiation is only an internal hazard.

Beta radiation (β)

Beta radiation consists of charged particles that are ejected from an atom's nucleus and that are physically identical to electrons. Beta particles generally have a negative charge, are very small and can penetrate more deeply than alpha particles. However, most beta radiation can be stopped by small amounts of shielding, such as sheets of plastic, glass or metal. When the source of radiation is outside the body, beta radiation with sufficient energy can penetrate the body's dead outer layer of skin and deposit its energy within active skin cells. However, beta radiation is very limited in its ability to penetrate to deeper tissues and organs in the body. Beta-radiation-emitting nuclear substances can also be hazardous if taken into the body.

Photon radiation (gamma [γ] and X-ray)

Photon radiation is electromagnetic radiation. There are two types of photon radiation of interest for the purpose of this document: gamma (γ) and X-ray. Gamma radiation consists of photons that originate from within the nucleus, and X-ray radiation consists of photons that originate from outside the nucleus, and are typically lower in energy than gamma radiation. Photon radiation can penetrate very deeply and sometimes can only be reduced in intensity by materials that are quite dense, such as lead or steel. In general, photon radiation can travel much greater distances than alpha or beta radiation, and it can penetrate bodily tissues and organs when the radiation source is outside the body. Photon radiation can also be hazardous if photon-emitting nuclear substances are taken into the body.

Neutron radiation (n)

Apart from cosmic radiation, spontaneous fission is the only natural source of neutrons (n). A common source of neutrons is the nuclear reactor, in which the splitting of a uranium or plutonium nucleus is accompanied by the emission of neutrons. The neutrons emitted from one fission event can strike the nucleus of an adjacent atom and cause another fission event, inducing a chain reaction. The production of nuclear power is based upon this principle. All other sources of neutrons depend on reactions where a nucleus is bombarded with a certain type of radiation (such as photon radiation or alpha radiation), and where the resulting effect on the nucleus is the emission of a neutron. Neutrons are able to penetrate tissues and organs of the human body when the radiation source is outside the body. Neutrons can also be hazardous if neutron-emitting nuclear substances are deposited inside the body. Neutron radiation is best shielded or absorbed by materials that contain hydrogen atoms, such as paraffin wax and plastics. This is because neutrons and hydrogen

atoms have similar atomic weights and readily undergo collisions between each other.

1.3.3 Natural sources of ionizing radiation

Radiation has always been present and is all around us in many forms. Life has evolved in a world with significant levels of ionizing radiation, and our bodies have adapted to it. The United Nations Scientific Committee on the Effects of Atomic Radiation (UNSCEAR) identifies four major sources of public exposure to natural radiation:

· Cosmic radiation

The earth's outer atmosphere is continually bombarded by cosmic radiation. Usually, cosmic radiation consists of fast moving particles that exist in space and originate from a variety of sources, including the sun and other celestial events in the universe. Cosmic rays are mostly protons but can be other particles or wave energy. Some ionizing radiation will penetrate the earth's atmosphere and become absorbed by humans which results in natural radiation exposure.

· Terrestrial radiation

The composition of the earth's crust is a major source of natural radiation. The main contributors are natural deposits of uranium, potassium and thorium which, in the process of natural decay, will release small amounts of ionizing radiation. Uranium and thorium are found essentially everywhere. Traces of these minerals are also found in building materials so exposure to natural radiation can occur from indoors as well as outdoors.

· Inhalation

Most of the variation in exposure to natural radiation results from inhalation of radioactive gases that are produced by radioactive minerals found in soil and bedrock. Radon is an odourless and colorless radioactive gas that is produced by the decay of uranium. Thoron is a radioactive gas produced by the decay of thorium. Radon and thoron levels vary considerably by location depending on the composition of soil and bedrock.

· Ingestion

Trace amounts of radioactive minerals are naturally found in the contents of food and drinking water. For instance, vegetables are typically cultivated in soil and ground water which contains radioactive minerals. Once ingested, these minerals result in internal exposure to natural radiation. Naturally occurring radioactive isotopes, such as potassium-40 and carbon-14, have the same chemical and biological properties as their non-radioactive isotopes. These radioactive and

non-radioactive elements are used in building and maintaining our bodies.

1.3.4 Artificial (man-made) sources of ionizing radiation

People are also exposed to man-made radiation from medical treatments and activities involving radioactive material. Radioisotopes are produced as a by-product of the operation of nuclear reactors, and by radioisotope generators like cyclotrons. Many man-made radioisotopes are used in the fields of nuclear medicine, biochemistry, the manufacturing industry and agriculture. The following are the most common sources:

- Medical sources: Radiation has many uses in medicine. The best-known application is in X-ray machines, which use radiation to find broken bones or to diagnose diseases. X-ray machines are regulated by Health Canada and provincial authorities. Another example is nuclear medicine, which uses radioactive isotopes to diagnose and treat diseases such as cancer.
- Industrial sources: Radiation has various industrial uses, which range from nuclear gauges used in the building of roads to density gauges that measure the flow of material through pipes in factories. Radioactive materials are also used in smoke detectors and some glow-in-the dark exit signs, as well as to estimate reserves in oil fields. Other applications include sterilization, which is performed using large, heavily shielded irradiators.
- Nuclear fuel cycle: Nuclear power plants (NPPs) use uranium to produce a chain reaction that produces steam, which in turn drives turbines to produce electricity. As part of their normal activities, NPPs release small quantities of radioactive material in a controlled manner to the surrounding environment. These releases are regulated to ensure doses to the public are well below regulatory limits.
- Atmospheric testing: The atmospheric testing of atomic weapons from the end of the Second World War until as late as 1980 released radioactive material, called fallout, into the air. As the fallout settled to the ground, it was incorporated into the environment. Much of the fallout had short half-lives and no longer exists, but some continues to decay. People and the environment receive smaller and smaller doses from the fallout every year.

1.3.5 Striking a balance

Normally, there is little we can do to change or reduce ionizing radiation that comes from natural sources like the sun, soil or rocks. This kind of exposure, while never entirely free of risk, is generally quite low. However, in some cases, natural sources of radioactivity – such as radon gas in the home – may be unacceptably high and need to

be reduced.

The ionizing radiation that comes from man-made sources and activities is controlled more carefully. In these settings, a balance is struck between radiation's societal benefits and the risks it poses to people, health and the environment. Dose limits are set to restrict radiation exposures to both workers and members of the public. In addition, licensees are required to keep all radiation doses as low as reasonably achievable (ALARA). There must also be a net benefit to support the use of radiation.

1.4 Radiation Doses

For the purpose of radiation protection, dose quantities are expressed in three ways: absorbed, equivalent, and effective. Figure 1-1 presents an overview of the relationship between effective, equivalent and absorbed doses [1].
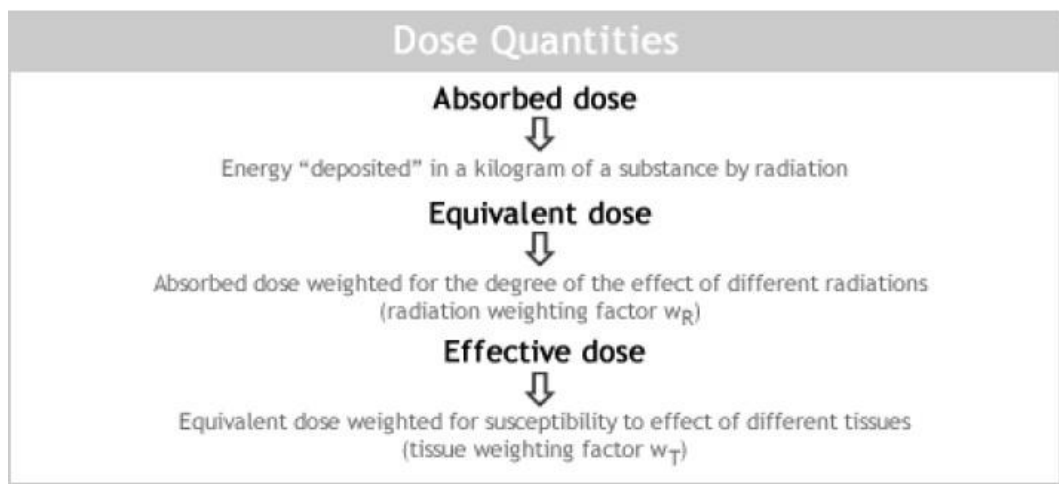
Fig. 1-1 Relationship between effective, equivalent and absorbed doses

1.4.1   Absorbed dose

When ionizing radiation penetrates the human body or an object, it deposits energy. The energy absorbed from exposure to radiation is called an absorbed dose. The absorbed dose is measured in a unit called the gray (Gy). A dose of one gray is equivalent to a unit of energy (joule) deposited in a kilogram of a substance.

<div align="center">

Old Unit: Rad; 1 Rad = 100 ergs/g

SI Unit: Gray (Gy); 1 Gy = 1 J/kg

1Gy = 100 Rads

</div>

1.4.2 Equivalent dose

When radiation is absorbed in living matter, a biological effect may be observed. However, equal absorbed doses will not necessarily produce equal biological effects. The effect depends on the type of radiation (e.g., alpha, beta or gamma). Different types of radiations have different rates of energy loss per unit of path length, which in other terms is referred to as Linear Energy Transfer (LET). For example, 1 Gy of alpha radiation is more harmful to a given tissue than 1 Gy of beta radiation. To obtain the equivalent dose, the absorbed dose is multiplied by a specified radiation weighting factor (W_R). A radiation weighting factor (W_R) is used to equate different types of radiation with different biological effectiveness. The equivalent dose is expressed in a measure called the sievert (Sv). This means that 1 Sv of alpha radiation will have the same biological effect as 1 Sv of beta radiation. In other words, the equivalent dose provides a single unit that accounts for the degree of harm that different types of radiation would cause to the same tissue.

$$H_T = \sum_R D_{T,R}.W_R$$

Where

H_T = Equivalent dose to tissue T; $D_{T,R}$ = Dose to tissue T because of radiation R; W_R = Radiation weighting factor. It is a dimensionless quantity;

<div align="center">

Old Unit: Rem; 1 Rem = 100 ergs/g

SI Unit: Sievert (Sv); 1 Sv = 1 J/kg

1 Sv = 100 Rems

</div>

1.4.3 Effective dose

Different tissues and organs have different radiation sensitivities (Fig. 1-2) [1]. For example, bone marrow is much more radiosensitive than muscle or nerve tissue. To obtain an indication of how exposure can affect overall health, the equivalent dose is multiplied by a tissue weighting factor (W_T) related to the risk for a particular tissue or organ. This multiplication provides the effective dose absorbed by the body. The unit used for effective dose is also the sievert.

$$E = \sum_T W_T.H_T$$

Where W_T = tissue weighting factor; H_T = equivalent dose to tissue T.
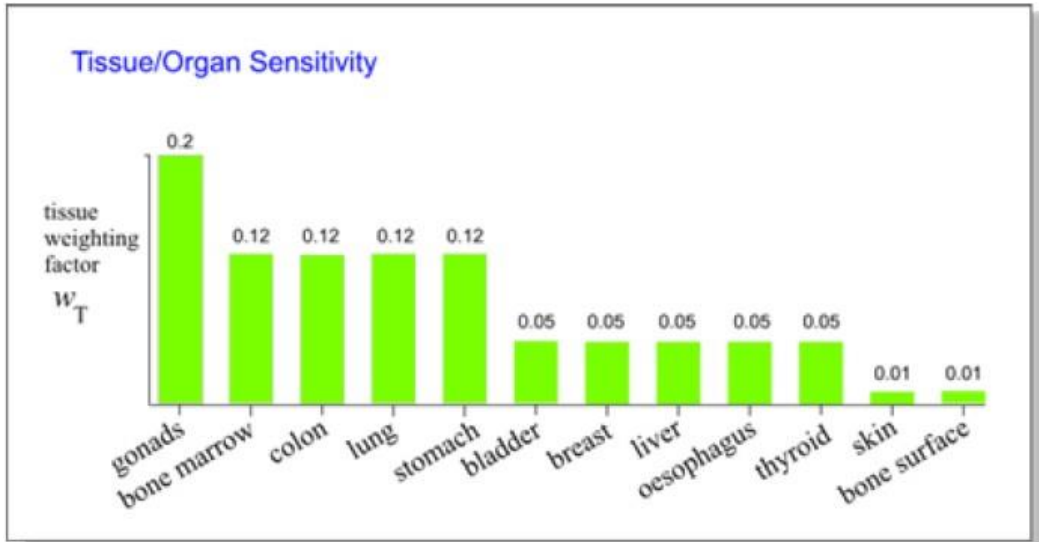
Source: *Radiation Protection Regulations.*

Fig. 1-2 Tissue weighting factors

1.4.4 Typical radiation doses

The total worldwide average effective dose from natural radiation is approximately 2.4 mSv per year; Man-made sources of radiation (from commercial and industrial activities) account for approximately 0.2 μSv of our annual radiation exposure. X-rays and other diagnostic and therapeutic medical procedures (Table 1-1) account for approximately 1.2 mSv a year (UNSCEAR 2000) [2]. There is no difference between the effects caused by natural or man-made radiation.

Study type	Relevant organ	Dose (mSv)
Dental X-ray[1]	Brain	0.01
Chest X-ray[1]	Lung	0.1
Screening mammography[2]	Breast	3.0
Adult abdominal CT[2]	Stomach	10.0
Neonatal abdominal CT[2]	Stomach	20.0

[1]National Council on Radiation Protection and Measurements (NCRP) 2009

[2]Brenner and Hall, 2007

Table 1-1 Typical equivalent doses from various radiological examinations

Chapter 2   Health Effects of Radiation Exposure

2.1 Biological Effects of Radiation

Radiation affects our health primarily through breakage of deoxyribonucleic acid (DNA) molecules. DNA is a long chain of amino acids whose pattern forms the blueprint on how a cell lives and functions, and radiation is able to break that chain. The damages to DNA chains may result in cell killing or modifications without loss of cell viability. Cell killing can result in deterministic effects, whereas cell modifications may give rise to stochastic effects.

2.1.1   Deterministic effects

When the DNA or other critical parts of a cell receive a large dose of radiation, the cell may die or be damaged beyond repair. If this happens to a large number of cells in a tissue or organ, early radiation effects may occur. These early effects are called "deterministic effects" and their severity varies according to the radiation dose received. They can include burns, cataracts and, in extreme cases, death.

2.1.2   Stochastic effects

In some cases, part of the DNA in the cell may be damaged by radiation and may not properly repair itself. The cell may continue to live and even reproduce itself. However, during that process, errors that have not been repaired in the DNA chain will also be present in the cell descendents and may disrupt these cells' functioning. This type of detrimental effect has a probability that is proportionate to the dose, and is called a "stochastic effect". The harmful effect most commonly of concern is radiation-induced cancer, which typically does not manifest itself until several years after the initiating exposure. Radiation carcinogenesis and hereditary effects are two important examples of stochastic effects of radiation and they originate from cell modifications.

2.2 The Risks

The word "safe" means different things to different people. For many, the idea of being safe is the absence of risk or harm. However, the reality is that almost everything we do presents a certain level of risk. For example, speed limits on roads are set to maximize safety. Nevertheless, accidents occur even when drivers obey the speed limit. Despite this risk, we still drive. Similar informed decisions are made when radiation is used. Radiation exposure carries a health risk. One significant advantage of radiation is

that more is known about its associated health risks than about any other chemical or otherwise toxic agent. Since the early 20th century, radiation effects have been studied in depth, in both the laboratory and among human populations.

2.2.1 Epidemiological evidence

Studies on survivors of the nuclear accident in history indicate that the principal long-term effect of radiation exposure is an increase in the frequency of cancer and leukemia.

Studies have shown that radiation will increase the frequency of some cancers that already occur naturally (or spontaneously), and that this increase is proportionate to the radiation dose; that is, the greater the dose, the greater the risk of cancer. These are referred to as stochastic effects. However, studies to date have not shown that people chronically exposed to radiation at doses lower than about 100 mSv per year will experience an increase in cancer or other diseases.

The following hypotheses attempt to explain why we cannot see radiation effects at doses of less than 100 mSv per year:

- One possible explanation is a dose threshold below which no cancers are caused; for example, radium has a threshold of 10 Sv for bone cancer.
- Another hypothesis is that the incidence of cancer caused by low radiation doses is so low that it cannot be distinguished from natural (or spontaneous) occurrences of the same cancer. This hypothesis is supported by studies of the National Academy of Biological Effects of Ionizing Radiation (BEIR) and the International Commission on Radiation Protection (ICRP).

2.2.2 Cancer risk assessment

The ICRP has calculated the probability of fatal cancer by relying primarily on the assessment of radiation effects by scientific bodies such as UNSCEAR and BEIR. It then determined what it calls the overall "detriment" of radiation exposure. This includes:

- the probability of fatal cancer
- the probability of non-fatal cancer
- the probability of severe hereditary effects
- the length of life lost if the harm occurs

Using all these risks, the ICRP calculated an overall detriment of 0.042 (4.2%) per sievert for adult workers and 0.057 (5.7%) per sievert for the overall population (ICRP 103). The risk for the overall population is slightly higher than that of workers due to

differences in certain variables, such as sex and age ranges, that were taken into account. Table 2-1 gives the breakdown of this summed figure into its constituent elements [3].

Detriment (10^{-2} Sv^{-1})	
Fatal cancer	5.0
Non-fatal cancer*	1.0
Severe hereditary effects	1.3
Total	7.3

*The lifetime probability co-efficient for non-fatal cancer represents detriment rather than true incidence, which would be significantly greater.

Table 2-1 Nominal lifetime probability coefficients for stochastic effects

Dose limits are set at a level below which the risk is regarded as acceptable. However, as a prudent measure, it is assumed that every exposure to radiation, even if under the dose limit, carries some risk; therefore, regulations require to reduce all doses to levels that are ALARA.

2.2.3 Risk in relation to age

Risk is age-dependent, being highest for the young and least for the elderly. It should be modified using the multiplication factors given in Table 2-2 [3]. These represent averages for the two sexes; at all ages risks for females are slightly higher and those for males slightly lower.

Age Group (years)	Multiplication factor for risk
<10	x 3
10-20	x 2
20-30	x 1.5
30-50	x 0.5
50-80	x 0.3
80+	Negligible risk

Table 2-2 Risk in relation to age

Beyond 80 years of age, the risk becomes negligible because the latent period between X-ray exposure and the clinical presentation of a tumor will probably exceed the life span of a patient. In contrast, the tissues of younger people are more radiosensitive and their prospective life span is likely to exceed the latent period.

2.2.4 Models to estimate the health risks

The linear non-threshold model (LNT) is a risk model used internationally by most health agencies and nuclear regulators to set dose limits for workers and members of the public. The LNT conservatively assumes there is a direct relationship between radiation exposure and cancer rates.

Several other risk models exist (Fig. 2-1), each with advantages and disadvantages [4]. They differ depending on the basis of their assumptions and whether they take uncertainty into account.
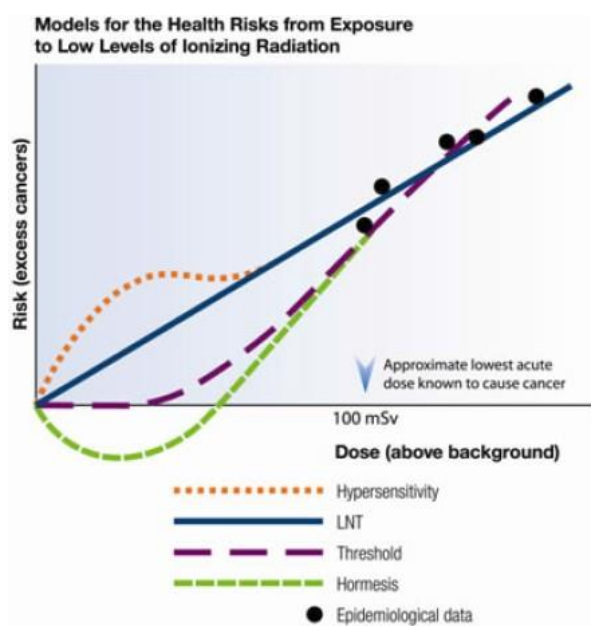
Fig. 2-1 Models to estimate the health risks from exposure to low levels of ionizing radiation (Source: Introduction to Radiation)

2.3 Dose Limits

Table 2-3 summarizes the potential health effects associated with given radiation doses [4]. Dose limits have also been included to illustrate how they protect workers and the public.

Dose (mSv)	Limit or Health Effect
$\geqq$ 5,000	Dose that may lead to death when received all at once
1,000	Dose that may cause symptoms of radiation sickness (symptoms include tiredness and nausea) if received within 24 hours
100	Lowest acute dose known to cause cancer
30–100	Radiation dose from a full-body computed axial tomography (CAT) scan
50	Annual radiation dose limit for nuclear energy workers
1.8	Average annual natural background dose
1	Annual public radiation dose limit in Canada
0.1–0.12	Dose from lung X-ray
0.01	Dose from dental X-ray
0.01	Average annual dose due to air travel

Table 2-3 Radiation doses, dose limits and potential health effects (Source: Introduction to Radiation)

2.4 Ways to Minimize Exposure

Ionizing radiation like gamma rays, X-rays can irradiate persons at a distance resulting in external radiation hazard. External radiation hazards can be controlled by the use of any or all the following three factors [5]:

2.4.1   Time

The total dose received by a person is directly proportional to the time spent near the radioactive source. Hence, minimize the time spent during handling or in the vicinity of radiation sources.

2.4.2   Distance

The exposure rate at any location follows inverse square law i.e. the exposure rate decreases as $1/R^2$, where R is the distance from the source.

$$\frac{X_2}{X_1} = \left[\frac{R_1}{R_2} \right]^2$$

Where X_1 is the exposure rate at distance R_1 and X_2 is the exposure rate at distance R_2.

Hence, maximization of distance from the source reduces the exposure level.

2.4.3　Shielding

Radiation is attenuated by different materials. Shielding of radiation makes use of this radiation attenuating property of different materials. Alpha particles are easily stopped by any matter, a few cm of air, less than an mm of water or paper or any other material. Most of the beta particles are stopped by a few mm of plastic, water or glass. X-rays and gamma rays are not easily stopped since they are highly penetrating and follow exponential attenuation law.

$$I = I_0 e^{-\mu t} = I_0 e^{-0.693t/HVT}$$

Where

I = transmitted intensity of radiation (after the shield)

I_0 = incident intensity (before the shield)

t = thickness of the shield (say in mm)

HVT = Half Value Thickness of the material (mm)

HVT represents the thickness of a material which is required to reduce a given intensity of gamma (or X) rays to half its initial value. HVT depends on the shield composition and the energy of the radiation. In general, (a) Higher the atomic number (Z) of the material, lower is the HVT (b) Higher the density, lower is the HVT and (c) Lower the energy of radiation, lower is the HVT. Better shield needs smaller HVT. Thus, lead is a good shielding material for gamma rays and X-rays. Hydrogenous materials such as water and paraffin make efficient neutron shields. Concrete and earth are also the shielding materials of choice for neutron source.

2.4.4　Other Principles

Although radiation exposures would make kinds of damages to human and environment, people often choose to accept irradiation because the benefits in medical application or inescapable reasons in nuclear accident. In these cases, the following principles should be paid more attention to [6]:

・ Low energy in diagnosis－lower energy of radiation beams make lower doses. For example, it is effective to reduce organ doses in CT examinations by making tube current or tube voltage lower when the diagnosis could be ensured.

・ Precisely delivery in treatment－make less doses in targets surrounding normal organs by concentrating beams on targets as possible as we can.

・ Decontamination in radioactive accident－remove radioactive materials from living environment surrounding people such as the decontamination work in Fukushima.

Section Ⅱ Protection in Paediatric CT

In this section, the reference radiation dose and organ doses from chest CT studies of children were estimated by using the data of clinical practice of a medical center in Japan. Moreover, organ doses and effects of thickness of superficial soft tissue to them in paediatric abdomen CT were also evaluate by use of a child anthropomorphic phantom

Chapter 3 Diagnostic doses based on patient's weight in paediatric chest CT: a 1-year retrospective review using a 64-slice CT scanner

3.1 Introduction and Objective

The use of CT has increased rapidly in the past two decades. CT is a powerful tool for the examination of chest disease because it can depict the disease process far more clearly than chest radiographs and is increasingly used for children [7-10]. The contributions of CT examinations to the collective dose from diagnostic radiation exposures have been estimated to be 67% in the United States and 47% in the United Kingdom [11, 12]. Currently, there has been revolutionary development in multidetector CT (MDCT) technology that has contributed to larger volume coverage with higher resolution and lower noise. However, this development has led to increased radiation exposure [7]. The radiation risks from CT have been recently reported in many studies [13, 14]. Caution should be exercised in the pediatric setting because children have higher radio-sensitivity due to more rapidly dividing cells than adults and a longer life expectancy [14]. In this study, the reference radiation dose and organ doses from chest CT studies of children were estimated by using the data of clinical practice of the National Center for Child Health and Development (NCCHD) in Japan.

   In composing local diagnostic reference doses and organ doses, the aim of this study was to provide a reliable and accurate data on the exposures in X-ray CT examinations for paediatric patients, which could be useful for optimization of radiation protection.

3.2 Materials and Methods
3.2.1   Materials of this review

   A retrospective review of children going through clinically indicated chest CT studies at the NCCHD was performed under the institutional review board approval. Two hundred and one clinical chest CT studies performed on 162 children (85 boys/77 girls, newborn to 15 years old in 2010) were reviewed. In this review, patient data including age (at the time of scan), gender, weight and clinical indication were collected. These examinations were chosen because they were the most common clinical examinations in the institution and provided statistically significant numbers. For the CT scan, the following parameters were extracted from the DICOM headers: (a)GE Discovery

750HD (GE Healthcare, Little Chalfont, UK); (b)tube voltage (kV); (c)tube current (mA); beam width; (d)rotation time and (e)pitch.

For each examining study, CT Dose Index Volume ($CTDI_{vol}$) of each CT scan was also extracted from DICOM header and the average value of $CTDI_{vol}$ of each protocol was also estimated. The basis for CTDI calculations in the GE CT scanner is that a 16-cm or 32-cm diameter PMMA phantom which is used to report the CTDI whenever a 'Ped Head' or 'Ped Body' Scan Field of View is selected [7].

3.2.2 Measurement of a child anthropomorphic phantom

In this study, radiation doses were measured with radiophotoluminescence glass dosemeters (RGD) set in various organ positions within a 6-year-old child anthropomorphic phantom and organ doses were evaluated from the measurement values. The CT scanner in this measurement was a GE LightSpeed RT CT scanner.

The RGD system, Dose Ace (Chiyoda Technol Co.LTD, Japan), is consisted of silver-activated phosphate glass dosemeters and an automatically readout system (FGD-1000) (Fig. 3-1-a). RGDs (Fig. 3-1-b) were annealed at 400℃ for 60 min and the initial values were read using FGD-1000. After X-ray beam irradiation, RGDs were healed at 70℃ for 30 min and were read using FGD-1000. RGD has two types of dosemeters: without energy compensation filters (GD-302M) and with tin filters (Fig. 3-1-c) for adjusting photon energy dependence (GD-352M). GD-302M was used in this study because the positions and holes for setting the dosemeters in the child phantom were only designed for this study. Moreover, GD-302M was calibrated with a traceable ionization chamber to the Japanese national standard at the Advanced Industrial Science and Technology (AIST). The RGDs and the ionization chamber were set in soft tissue equivalent slab phantoms and irradiated X-ray beam of various energies. The readout values of RGDs were converted into absorbed doses for tissues or organs using the conversion factors obtained from the calibration.

a

b

c

Fig. 3-1 The RGD system, Dose Ace - FGD-1000, RGDs and tin filters.

The phantom used in this study was produced by Kyoto Kagaku co., LTD in Japan. It represents the average body size of 6-year-old child, 20 kg in weight and 115 cm in height (Fig. 3-2). The phantom is composed of tissue equivalent substitutes corresponding to soft tissue, lung and bone, and divided into 25 mm thick axial slices (Fig. 3-3). In total, 172 RGDs were set at the positions of tissues or organs. These sites of tissues or organ were determined in consultation with medical staff including a paediatrician.
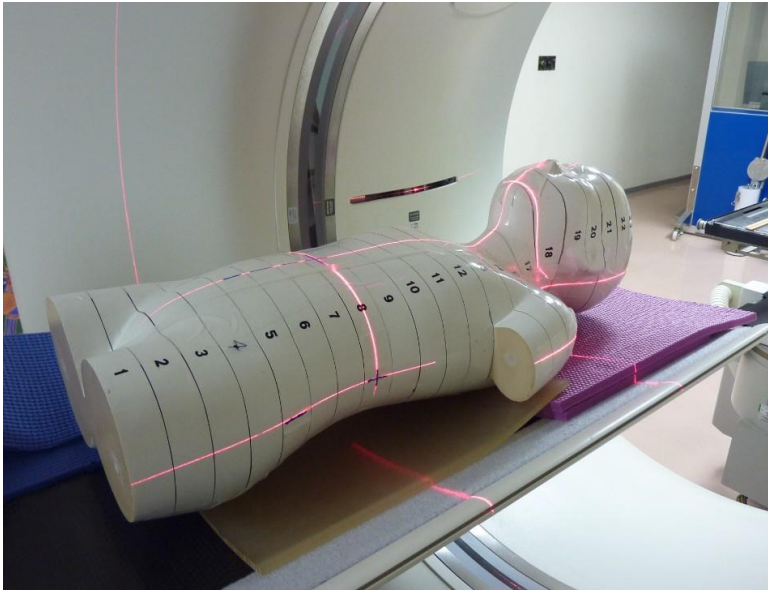
Fig. 3-2 The 6-year-old child phantom was set upon the CT plate.

Fig. 3-3 One of the thick axial slices of the phantom.

3.2.3 CT-Expo Simulation

The $CTDI_{vol}$ and organ doses of typical examine cases were evaluated also by use of CT-Expo, which is a professional MS Excel application for assessing the radiation doses delivered to patients undergoing CT examinations based on the simulations, and used to analyze the data collected in the German survey on CT practice. The program enables the calculation of all dose quantities of practical value, such as axial dose free-in-air, weighted CTDI, dose-length product, effective dose and uterine dose. In contrast to

existing programs for CT dose assessment, CT-Expo offers a number of unique features, such as gender-specific dose calculation for three typical age groups (adult, children, newborn), applicability to all existing scanner models including correction of scanner-specific influences, and the possibility of comparison with the results from the German CT survey on CT practice. Three different application modules offer free and standardized dose calculations as well as a comprehensive benchmarking section including guidance on dose optimization [20].

CT-Expo offers a 57-cm-height, 4.2-kg-weight baby phantom and a 115-cm-height, 22-kg-weight child phantom for dose simulation. The scanner in the facility provides a modulation of the tube current along the z-axis according to the local attenuation properties of the patient (longitudinal dose modulation). However, the average tube current is not available, so that the effective mAs was not reported. Therefore, the dose-length product (DLP) displayed at the operator's console were used varying the mAs product until the DLP value calculated with CT-Expo is the same as at the console. A 55-cm-height, 4.3-kg-weight baby (patient A) and a 115-cm-height, 21-kg-weight child (patient B) who has gotten a typical chest CT scan was selected from the data base for reference dose calculation, and the computed organ doses of patient B were compared with the results of phantom measurement.

3.3 Results and Discussion

3.3.1　Basic information and CTDIs of this review

The average age of the children in this study was 4.7±4.7 years with a range from newborn to 15 years (Fig. 3-4). In addition, the weights of the children (at the time that they underwent CT scans) ranged from 2.5 to 90.3 kg, with an average of 16.3±13.6 kg. The average number of chest CT studies was 1.2 per patient (range: 1-5 times). The number of patients corresponding with the number of studies was reviewed and showed in Fig. 3-5. The organs and the diseases that were required to be examined in this review were counted and shown in the Figure 3-6 and Figure 3-7, respectively. In the total 201 scans, 120 scans (60%) of non-contrast CT, 64 scans (32%) of contrast CT, and 17 scans (8%) of chest CT angiography (CTA) were respectively operated. According to the clinical statistics, on the one hand, there were 90 scans (45%) for lungs, 34 scans (17%) for thorax, 16 scans (8%) for trachea, 13 scans (7%) for heart, 11 scans (5%) for diaphragm, and 27 scans (18%) for others. On the other hand, from the view of disease, 68 scans for tumor, 45 scans (22%) for phlegmasia, 44 scans (22%) for malformation/defect, and 44 scans (22%) for others were applied. As the most of the examinations were carried out for checking lungs or thorax and for checking tumor,

31

phlegmasia or malformation/defect that probably suffer in infant period, it was suggested the fact of that led the young-age-distribution of patients in the NCCHD.
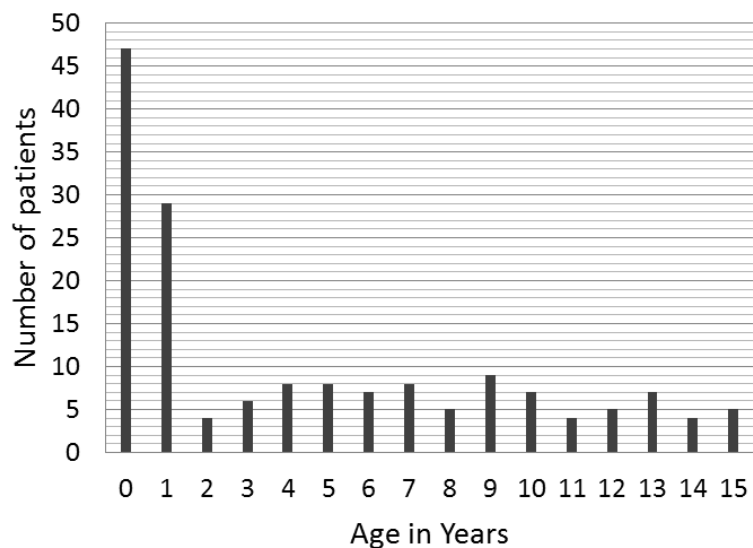
Fig. 3-4 Age distribution
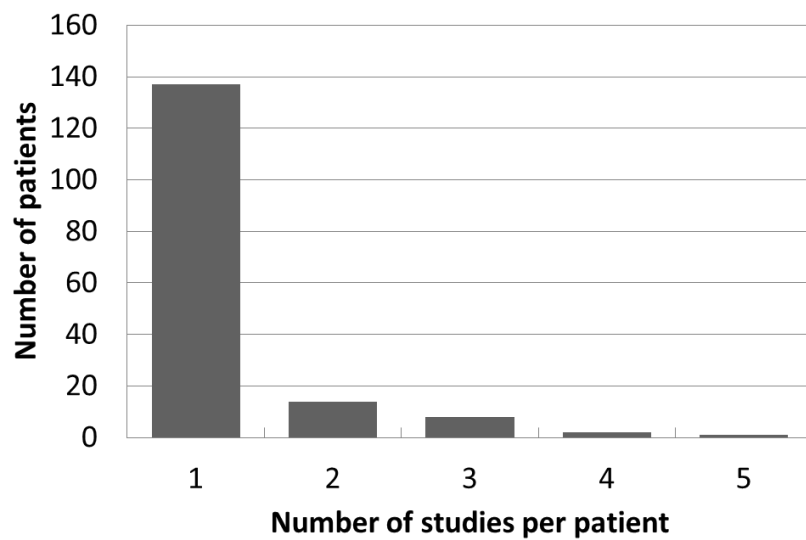
Fig. 3-5 Number of studies per patient
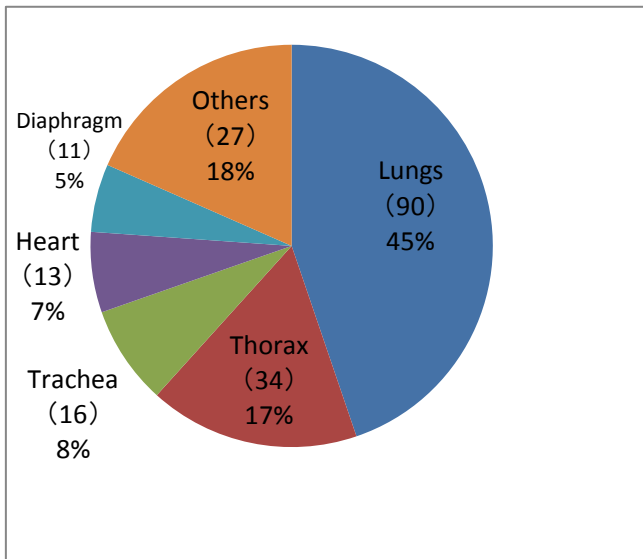
Fig. 3-6 The organs that were required to be examined in this study
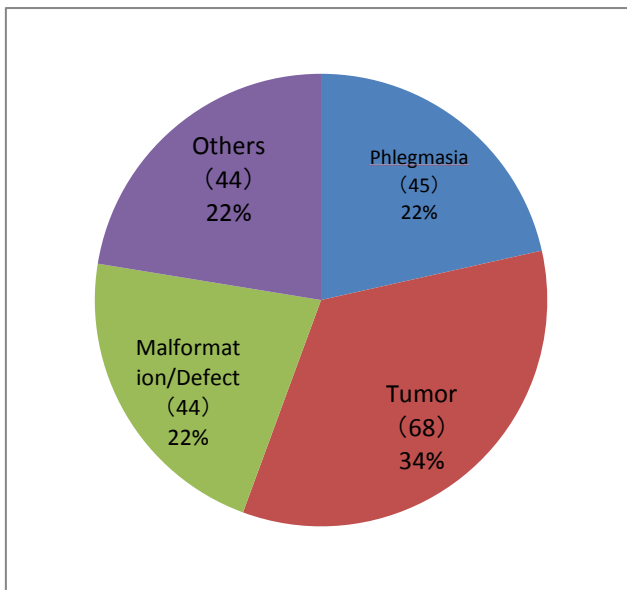
Fig. 3-7 The diseases that were required to be examined in this study

All of the examinations were implemented by a GE Discovery 750HD CT scanner. The typical parameters for chest CT studies were: 120 kVp (used for non-contrast and contrast CT scan) or 80 kVp (only used for CT angiography scan), upper limit of cube current range from 40 to 200 mA while Automatic Exposure Control (AEC) was used, rotation time of 0.4 s, helical pitch of 1.375 and beam width of 40 mm. The protocols of examinations, which are called color-coded CT protocols in the medical center, are summarized in Table 3-1. The protocols were established according to the

Broselow-Luten pediatric color-coded system by GE Healthcare. This system uses a color assignment based on the length or weight of a child [23, 24]. The appropriate support equipment (such as endotracheal tube size), correct medication doses, and IV fluid volumes are predetermined for each color zone. This method has been shown to substantially reduce the error rate in the emergency stabilization of infants and children in which care (i.e., range of sizes) can also be complicated. The number of color code in the protocols ranges from 1 to 9 for both of non-contrast CT scan and contrast CT scan. However, chest CTA scan is usually implemented in only two color codes. The chest protocols are used for children with typical presentations of malignancy, trauma, congenital malformations or infection. The tube current of each group for non-contrast CT scan, contrast CT scan and chest CT angiography scan protocols are also presented in the table.

Color Code Number	Scan Type	Non-contrast(120kV) Max mA	Contrast(120kV) Max mA	Chest CTA (80kV) Max mA
1	6.0-7.5 kg (59.5-66.5 cm)	40	60	70
2	7.5-9.5 kg (66.5-74.0 cm)	40	60	85
3	9.5-11.5 kg (74.0-84.5 cm)	45	65	-
4	11.5-14.5 kg (84.5-97.5 cm)	60	70	-
5	14.5-18.5 kg (97.5-110.0 cm)	60	80	-
6	18.5-22.5 kg (110.0-122.0 cm)	65	85	-
7	22.5-31.5 kg (122.0-137.0 cm)	90	110	-
8	31.5-40.5 kg (137-150.0 cm)	120	140	-
9	40.5-55.0 kg	180	200	-

Table 3-1 Tube current and weight of each color code in CT examination protocol of the national medical center

The corresponding average age and weight of each group in this review is shown in Table 3-2, with the sample number of each group is also reported. To consider the local diagnostic reference dose of the chest CT examinations, the mean values of $CTDI_{vol}$ of each group are reported in Figure 3-8. The 16-cm-diameter CT dosimetry phantom is used as the reference from group 1 to group 3, and the 32-cm-diameter CT dosimetry phantom is used in the other groups. Since the diameter of CT dosimetry phantom was changed from 16 cm to 32 cm group 4, a decrease of $CTDI_{vol}$ was shown between group 3 and group 4, and the discrepancy of $CTDI_{vol}$ between non-contrast scans and contrast scans was also decreased because of that. Moreover, it is also suggested that the increase in tube current causes fewer decrease in $CTDI_{vol}$ when the 32-cm-diameter CT dosimetry phantom is used.

Color Code Number	Non-contrast CT Scan (SD10)			Contrast CT Scan (SD8)			Chest CTA Scan		
	Sample size	Weight range (kg)	Average age (years)	Sample size	Weight range (kg)	Average age (years)	Sample size	Weight range (kg)	Average age (years)
1	18	2.8-7.2	0.1	18	2.5-7.5	0.2	14	2.5-6.4	0.2
2	15	7.4-9.4	1.0	8	7.7-9.4	0.6	3	8.0-9.4	0.7
3	10	9.5-11.2	1.6	8	9.6-11.2	1.5	-	-	-
4	13	9.5-15.5	5	9	10.8-14.3	3.1	-	-	-
5	19	14.7-17.9	6.9	5	14.7-17.9	5.2	-	-	-
6	12	18.0-22.2	8.2	5	19.0-20.7	7.4	-	-	-
7	12	22.9-29.0	10.5	8	22.3-31.4	9.3	-	-	-
8	7	32.1-40.0	12.1	1	34.0	9	-	-	-
9	14	40.6-68.0	12.8	2	41.2-90.3	15	-	-	-

Table 3-2 The corresponding sample size, weight, and average age of each color code
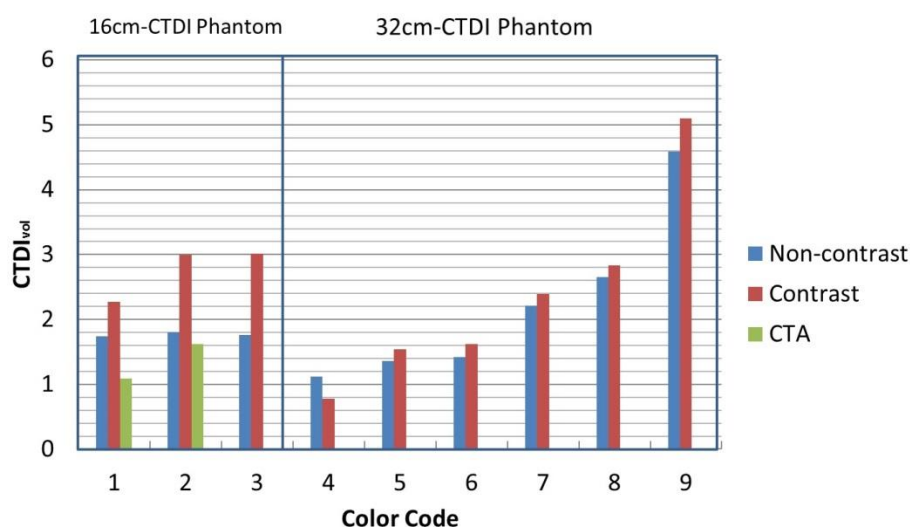
Fig. 3-8 The value of $CTDI_{vol}$ of different color code in each scan

With an increasing professional and public awareness of the future risk associate with ionizing radiation in medical imaging has come a growing discussion of the need for improved dose records. The relatively higher radio-sensitivity of children and the greater number of years in their future makes this of particular relevance in pediatric practice. The radiation exposure from CT studies is considerable, especially for those children patients comparing with adults. Children are a few times more sensitive than adults to the induction of cancer, and the increase of appropriate and inappropriate examinations with high radiological dose in children has raised concern among the pediatric community and regulatory bodies [19].

According to this review, about 50% of the children who underwent chest CT exposure were less than 2 years old, either male or female. Abstractly, many biological damages caused by absorbed radiation dose in this age period might lead to ailment or injury in their future. Moreover, it is found that most of the children were irradiated only once but the patients who underwent chest CT scan more than one time are almost patients of malignancies and went on to have radiation therapy follow-up.

Radiation doses in children CT examinations varied widely by the differences in the types of CT scanners and scan parameters used at each medical facility [15]. Children also vary dramatically in size for the same age group, particularly in the toddler and teenage years. These differences in body habitus affect the scan length and radiation dose delivered to achieve the same image quality. It is widely acknowledged that CT scanning should be performed using weight-based protocols [16-18].

$CTDI_{vol}$ and DLP have been proposed as the appropriate dose quantities for the establishment of diagnostic reference levels (DRLs) for promoting patient protection

from CT scan. In this review, the CTDI$_{vol}$ in contrast CT scan showed generally higher value than in non-contrast CT scan; in addition, CTA scan made the lowest radiation exposure dose by using lower tube voltage in practices. In general, CT scans would cause higher exposure doses as children getting more weight and using higher tube current in examinations, no matter what kind of scan. As Debbie Watson et al. has shown [7], on the one hand, mean values of CTDI$_{vol}$ in their study were 3, 3, and 5 in 0－10kg, 11－25kg, and 26－40kg group respectively, with the 16-cm-diameter CT dosimetry phantom as the reference. On the other hand, the values were 3, 4, 7, 9, and 16 in 11－25kg, 26－40kg, 41－60kg, 61－75kg and above 75kg group respectively with the 32-cm-diameter CT dosimetry phantom as the reference. Shrimpton [8] et al. has also shown that the CTDI$_{vol}$ of chest CT were ranged from 12 to 20 for patients who were under 10 years old in UK. Compare with their study, this review shows lower exposure dose of chest CT scan in Japan.

Singh [17] et al. has also shown the resultant radiation dose reduction with new pediatric chest CT protocols based on patient weight, clinical indication, number of prior CT studies, and AEC. For chest CT, there was 52.6% (9.1 vs 19.2 mGy) to 85.4% (2.8 vs 19.2 mGy) dose reduction in the implementation compared with dose at noncompliant examinations (P < .001); there was no loss of clinically relevant image quality.

3.3.2　Organ doses in the simulation and measurement

Scan parameters and organ doses in the simulation and the measurement are summarized in Table 3-3. In the chest CT, doses in organs such as the thyroid, lung and oesophagus in the scan range were 2.4－3.0 mGy with the use of GE Discovery 750HD Scanner (CT-Expo simulation), and those were 4.3－5.6 mGy with GE LightSpeed RT (measurement). Organ doses and effective doses for children in each CT protocol were reported in the previous papers. Fujii [21] et al. reported that doses for organs within the scan range in a chest CT for 6-year-old children with various types of 64 MDCT scanners were 4－17 mGy. Huang [22] et al. evaluated radiation doses in a cardiac CT with a 64 MDCT scanner; the doses for the lung, breast and oesophagus were 16－29 mGy. The doses in a cardiac CT for infants were less than three-fourth of those for children.

Evaluation method	CT-Expo	Phantom measurement
Tube voltage (kV)	120	120
Maximum tube current (mA)	—	65
Rotation time (s rot^{-1})	0.4	1
Pitch factor	1.375	1.5
Effective mAs	20.7	—
Scan length (cm)	23	25
Organ dose (mGy)		
Brain	0.3	0.3
Lens	2.5	0.2
Salivary glands	2.6	1.6
Thyroid	3.0	5.4
Lungs	2.5	4.8
Oesophagus	2.4	4.3
Mammary gland	2.8	5.6
Liver	2.2	2.4
Stomach	1.9	1.9
Colon	0.5	0.3
Ovaries	0.1	0.1
Bladder	0.0	0.0
Testes	0.0	0.0
Red bone marrow	0.6	—
Bone surface	2.5	—
Skin	0.8	—

Table 3-3 Scan parameters and organ doses in the simulation and the phantom measurement

According to the results and previous studies, different scan parameters and CT scanner would lead to significant differences in organ doses in paediatric chest CT scans. To patients with similar body sizes, scan parameters in different facilities are often different. Even the same scan parameters were used for the same patient, diagnostic organ doses might be discrepant when the examinations were implemented with different CT scanners since different X-ray effective energy. In the practices of the NCCHD, while the most of parameters are the same, the upper limit of tube current used at the facility with Discovery 750HD was adjusted to patient's weight and to whether contrast

medium was required or not.

3.3.3 Reference dose report by use of CT-Expo

Table 3-4 shows the scan parameters and the CTDIs that were reported in DICOM data and were calculated by use of CT-Expo. According to the results, $CTDI_{vol}$ that reported by the CT scanner and CT-expo is almost the same, especially for the child case. Therefore, it is reliable to evaluate organ doses by use of CT-Expo simulation for the child in typical body size.

	Data Base		CT-Expo	
Patient	A	B	A	B
Tube voltage (kV)	120	120	120	120
Maximum tube current (mA)	60	110	—	—
Rotation time (s rot^{-1})	0.4	0.4	0.4	0.4
Pitch factor	1.375	1.375	1.375	1.375
Effective mAs	—	—	21.3	20.7
$CTDI_{vol}$ (mGy)	2.83	2.44	2.50	2.40

Table 3-4 Scan parameters and CTDIs for typical cases in paediatric chest CT

For the patient A, the individual $CTDI_{vol}$, either reported from data base or simulated by use of CT-Expo, was almost the same as the average value of the group 1 in contrast CT which including the patient. As the contrast, since the upper limit of tube current was higher than the group 6 which the patient B was in, the individual $CTDI_{vol}$ was higher than the average value. Tube current, tube voltage or other parameters would be often decided to be different with group protocol in practice, no matter that was classified by patient's weight or age.

3.4 Conclusion

A set of CTDIs and organ doses in paediatric chest CT scan was compiled for the National Center for Child Health and Development based on children's weights. This enables easy reference by both radiographers and radiologists during routine clinical practice, and allows comparison with other published reference doses as a quality measure. These data will be continually reviewed and, as more comprehensive information are provided, quality improvement and benchmarking will be an integral part of quality improvement activities and dose optimization.

Chapter 4 Effect of Subcutaneous Soft tissues on Paediatric Abdominal-Pelvic MDCT Exposure Dose: Phantom Study

4.1 Introduction and Objective

The use of CT has increased rapidly in the past two decades. CT is a powerful tool for the examination of chest disease because it can depict the disease process far more clearly than chest radiographs and is increasingly used for children [25-27]. Moreover, Multi-detector row CT (MDCT) scanners have made remarkable advances in the past few decades, contributing to a substantial increase in its diagnostic applications and accuracy [28,29]. Radiation doses from diagnostic CT scan account for the largest contribution of radiation to the general public. However, radiation doses are often estimated from all diagnostic radiologic procedures based on values derived from a representative normal-weight "Reference Child/Man" whose anatomic characteristics no longer reflect those of the general population [30-32]. In this chapter, we described our investigation of radiation doses to overweight and obese children from diagnostic paediatric abdominal-pelvic MDCT examinations by the use of an anthropomorphic child phantom. The purpose was to evaluate the effect of abdominal subcutaneous soft tissues on organ and effective doses in paediatric abdominal CT examination.

4.2 Materials and Methods

In this study, radiation doses were measured with radiophotoluminescence glass dosemeters (RGD) set in various organ positions within a 6-year-old child anthropomorphic phantom and organ doses were evaluated from the measurement values. The CT scanner in this measurement was a GE LightSpeed RT 8 CT scanner.

4.2.1 GE LightSpeed RT 8 CT scanner

The GE LightSpeed RT 8 CT scanner (Fig. 4-1) was one of the world's first 8-Slice per rotation CT Scanners. With 8-Slices per second it is up to three times faster than 4-slice. The popular world-wide demand for this model was due partially by better paediatric exams, up to 30% less dose, revolutionary OptiDose® features, along with, breakthrough cardiovascular imaging and analysis applications.

Fig. 4-1 GE LightSpeed RT 8 CT scanner

4.2.2   The RGD system

The RGD system, Dose Ace (Chiyoda Technol Co.LTD, Japan), is consisted of silver-activated phosphate glass dosemeters and an automatically readout system (FGD-1000) (see Fig. 3-1). RGDs were annealed at 400℃ for 60 min and the initial values were read using FGD-1000. After X-ray beam irradiation, RGDs were healed at 70℃ for 30 min and were read using FGD-1000. RGD has two types of dosemeters: without energy compensation filters (GD-302M) and with tin filters for adjusting photon energy dependence (GD-352M). GD-302M was used in this study because the positions and holes for setting the dosemeters in the child phantom were only designed for this study. Moreover, GD-302M was calibrated with a traceable ionization chamber to the Japanese national standard at the Advanced Industrial Science and Technology (AIST). The RGDs and the ionization chamber were set in soft tissue equivalent slab phantoms and irradiated X-ray beam of various energies. The readout values of RGDs were converted into absorbed doses for tissues or organs using the conversion factors obtained from the calibration.

4.2.3   Anthropomorphic phantom

The phantom used in this study was produced by Kyoto Kagaku Co., LTD in Japan. It represents the average body size of 6-year-old child, 20 kg in weight and 115 cm in height (see Fig. 3-2). The phantom is composed of tissue equivalent substitutes corresponding to soft tissue, lung and bone, and divided into 25 mm thick axial slices

(Fig. 4-2). In total, 172 RGDs were set at the positions of tissues or organs. These sites of tissues or organ were determined in consultation with medical staff including a paediatrician.

Fig. 4-2 One of the thick axial slices of the phantom.

4.2.4　Flat layers of soft-tissue-equivalent material

The flat layer material is composed of soft tissue equivalent substitutes corresponding to subcutaneous soft tissues which are the same as that in the child anthropomorphic phantom. The material was produced by Kyoto Kagaku Co., LTD in Japan. The model of this material is XUR-SZ-207. It is made from urethane resin and divided into $300 \times 300 \times 5$ mm thick square slices. The state of the material in the experimental room is shown in Fig 4-3.

Fig. 4-3 The flat layers of soft-tissue-equivalent material

4.2.5 Methods and protocols of the measurements

In this study, the absorbed dose in each organ in paediatric abdominal-pelvic CT was evaluated by using the child anthropomorphic phantom. To individual differences, since a child generally has less internal organs fat than an adult, it is supposed that there is relatively little individual difference of the relative position of organ in the body. It was intended to evaluate organ doses by the difference in thickness of subcutaneous soft tissues.

Organ doses were measured by wrapping the anthropomorphic phantom with (0- in the tables and figures) and without (3- in the tables and figures) three slices (15 mm in thickness) of the soft-tissue-equivalent material in abdominal region. One slice of the material was put in the back side (Fig. 4-4). Each set was scanned under the automatic exposure control (AEC-on) and out of tube current modulation (AEC-off), respectively.


Fig. 4-4 The state of the child phantom wrapping with the layers of the material

The scan parameters are shown in Table 4-1, and the scan range is shown in Fig. 4-5. Parameters and scan range of general paediatric abdominal-pelvic were used in the measurements. Ten slices of phantom numbered from 2 to 11 were contained in the scan range. Organ doses were evaluated and analyzed according to the results.

| CT Scanner	LightSpeed RT 8	Scan Pattern	Helical
Bowtie Filter	Body	FOV	40 cm
Rotation time	1 s/rot	Pitch	1.5
Beam Width	20 mm	Tube voltage	120 kV
Tube Current	Max 120 mA (AEC-on SD 8)		120 mA (AEC-off)

Table 4-1 The scan parameters
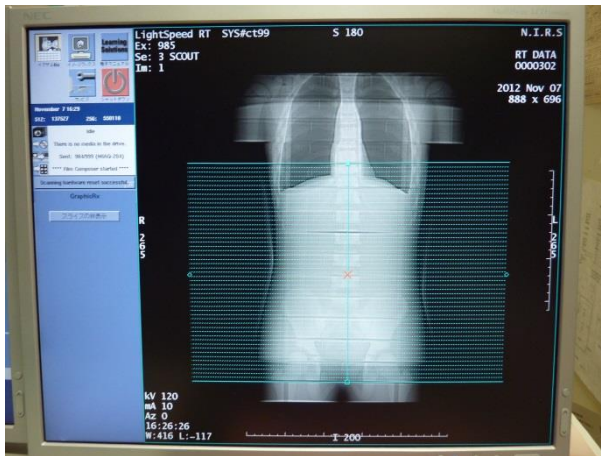
Fig. 4-5 The scan range

4.3 Results and Discussion

4.3.1　Organ doses

Organ doses in the paediatric abdominal-pelvic CT are shown in Fig. 4-6. According to the results, doses for the mammary glands, stomach, kidneys and ovary within the scan range were respective 9.4, 6.7, 6.7 and 7.2 mGy in the scan without the material and with tube current modulation (0-AEC on), which would be general in clinic practices. Comparing with the general scan, since the tube current increased by the use of AEC, organ doses except the mammary glands increased by 47% in the average after 15 mm soft tissues are wrapped in the abdominal region of phantom (3-AEC on). Among the organs, the liver dose increased from 6.2 mGy to 10.3 mGy at the max percentage of 65%. Although the tube current increased, the mammary glands dose decreased because the increase of the soft tissue thickness made the mammary glands out of the build-up region and the absorbed doses decreased. When the reference phantom was scanned without the AEC (0-AEC off), the organ doses were increased by 127% in the average. The stomach dose was increased to 19.3 mGy at the max percentage of 188% and the spleen dose reached the max value of 20.1 mGy in the measurements. Even though the soft tissue materials induced an increase in the tube current, the organ doses still showed a 35% decrease in the average comparing to the case of the materials wrapping on the phantom without the AEC (3-AEC off).
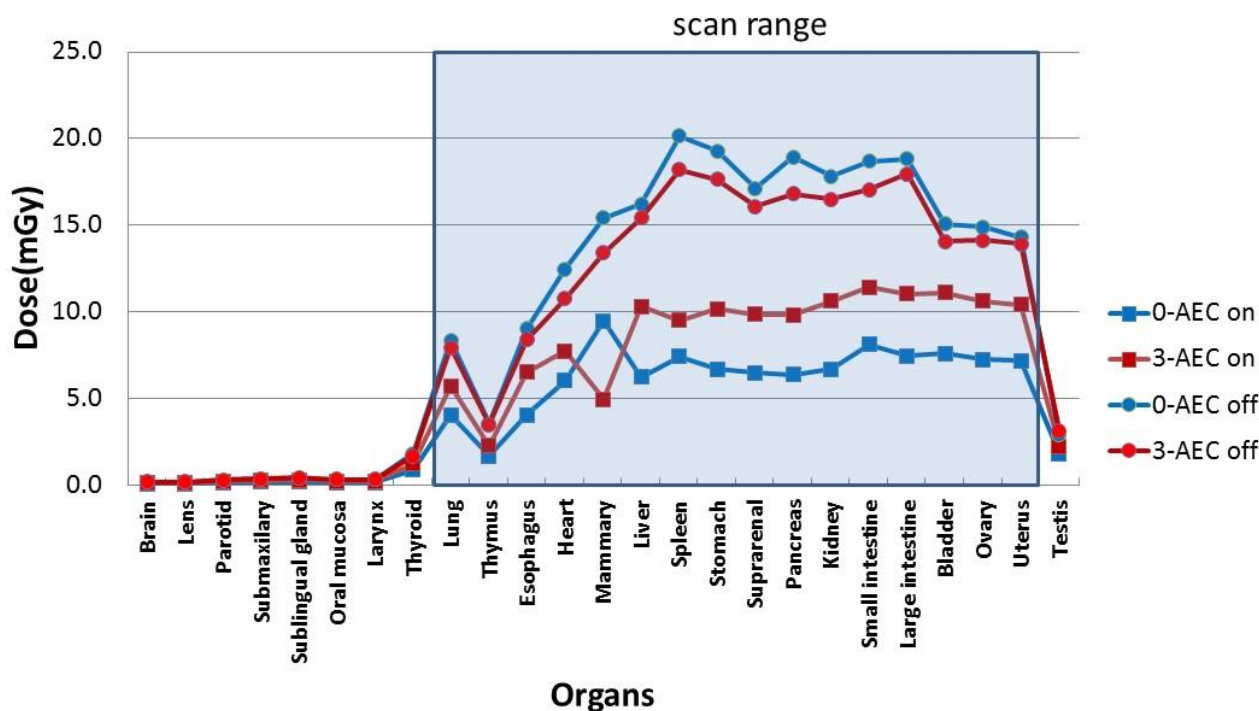
Fig. 4-6 Organ doses in the measurements

In the previous studies, Lee [33] et al. investigated the effect of abdominal subcutaneous fat on organ doses in abdominal CT examination by using deformable hybrid anthropomorphic phantoms and MCNPX2.5. They reported that as waist circumference increases, the thickness of abdominal subcutaneous fat increases correspondingly which causes a decrease in the organ absorbed dose for CT beams, especially, for the small intestinal wall (−5.8%) and kidney (−7.3%). It is suggested that even though the effect of fat thickness on organ dose was not significant in newborn phantom, higher correlation would be observed in older and larger phantoms. To the contrary, Schindera [34] et al. evaluated the effect of patient size on radiation dose for abdominal MDCT with automatic tube current modulation in a phantom study. They reported that with two protocols, in comparison with the dose of the small patient, the abdominal organ doses of the average-sized patient and the oversized patient increased 161.5–190.6% and 426.9–528.1%, respectively. The skin dose increased as much as 268.6% for the average-sized patient and 816.3% for the oversized patient compared with the small patient.

The doses for lung, thymus, esophagus and heart were averaged from the doses of measure points. However, there were only parts of them in the scan range, and the doses of those positions were similar to the organs in the fact. The testis was attached to the phantom as an accessory out of the scan range.

46

4.3.2 Effect of tube current modulation on organ doses

The application of tube current modulation in this study is called SmartmA system. SmartmA is an automatic exposure control system that employs Z axis tube current modulation and is available on all GE LightSpeed scanners. A noise index parameter allows you to select the amount of x-ray noise that will be present in the reconstructed images [35]. Using a single patient scout exposure, the last scout taken, CT system computes the required mA to be used based on the selected noise index setting. The noise index value will approximately equal the standard deviation in the central region of the image when a uniform phantom (with the patient's attenuation characteristics) is scanned and reconstructed using the standard reconstruction algorithm. The mA Table reports what the mA will be for each scan rotation in lateral (X) and anterior-posterior (Y) direction, based on the factors you have set on the SmartmA Control.

In this study, the tube current per each scan rotation in the modulated scans is shown in Fig. 4-7. According to the results, the tube current in the X-direction was always higher than it in the Y-direction. It is suggested that the transversal section of the phantom has a long Y-axis and a short X-axis as an ellipse. X-ray photons need to penetrate more tissues to reach the detectors in the X-direction. After wrapping the average-size phantom with the soft tissue materials, the tube current increased nearly 30 mA per each rotation, either in the X-direction or in the Y-direction. It is the directly reason of the increase of organ doses. However, the tube current is not only related to the thickness of the phantom, it is also related to the attenuation rate of materials. As shown in the figure, since the abdomen has much few bones than pelvis, there was a low-tube-current region in the area where the abdominal region was.
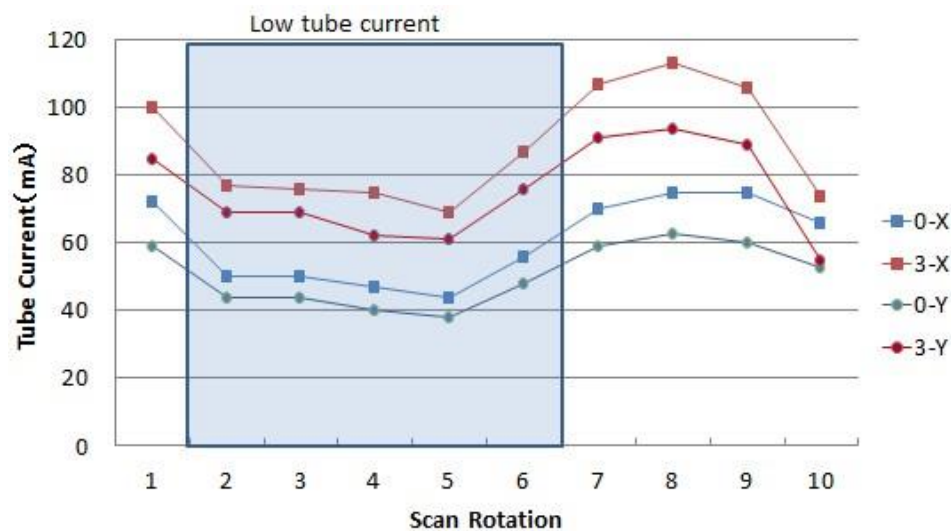

Fig.4-7 The tube currents of slices in table of Smart mA

The organ doses in the measurements are shown in the Table 4-2 while the organs in the low-tube-current region are marked with red ink. The average organ dose in the abdomen was evaluated to be 0.9 mGy lower than that in the pelvis with the use of AEC, either the soft-tissue materials wrapped (12% off) or not (8% off). In the contrast, the average dose was evaluated to be 1.9 mGy and 1.4 mGy higher than that in the pelvis with no use of the AEC, when the materials wrapped (12% up) or not (9% up), respectively.

Organs	0-AEC on (mGy)	3-AEC on (mGy)	0-AEC off (mGy)	3-AEC off (mGy)
Liver	6.2	10.3	16.2	15.4
Spleen	7.4	9.5	20.1	18.2
Stomach	6.7	10.2	19.3	17.6
Suprarenal	6.5	9.8	17.1	16.0
Pancreas	6.4	9.8	18.9	16.8
Kidney	6.7	10.6	17.8	16.5
Small intestine	8.1	11.4	18.7	17.0
Large intestine	7.4	11.0	18.8	17.9
Bladder	7.6	11.1	15.0	14.0
Ovary	7.2	10.6	14.9	14.1
Uterus	7.2	10.4	14.3	13.9

**Table 4-2** Organ doses in the scan range

4.3.3 The relation between organ depth and organ dose

To analyze the relation between the organ depth and organ dose, we measured each depth of measure point (in the direction that from the skin to helical center) in each slice of phantom. The depth of measure points in each slice is shown in Fig. 4-8, and Fig. 4-9 shows the measured dose of each point in the scans for the reference phantom without soft-tissue materials. According to the results, it is generally demonstrated that the measure point is deeper and the absorbed dose is lower, either in the AEC-off scan or in the AEC-on scan. Comparing to the AEC-on scan, the point dose in the AEC-off scan was more easily to be affected by the point depth.
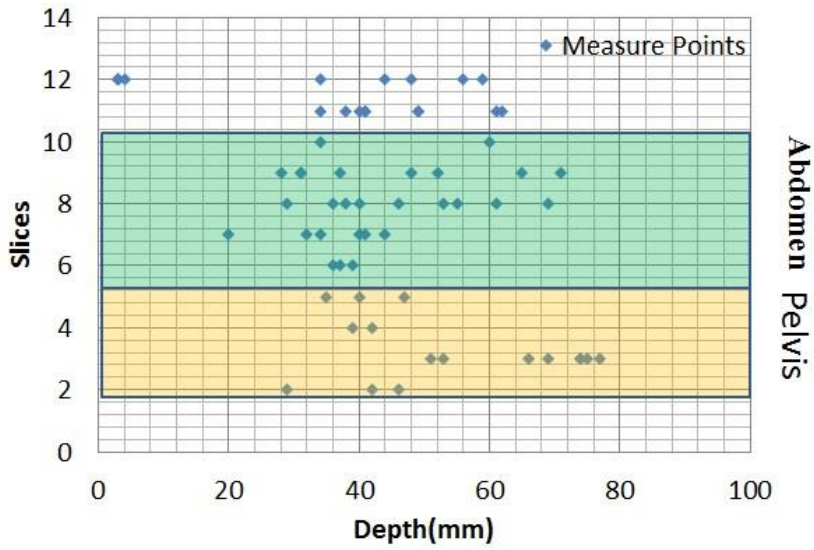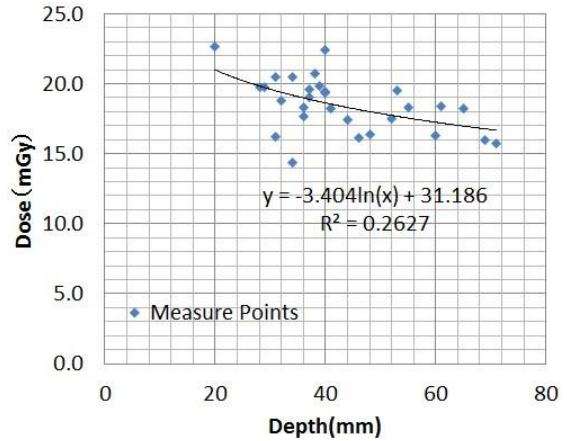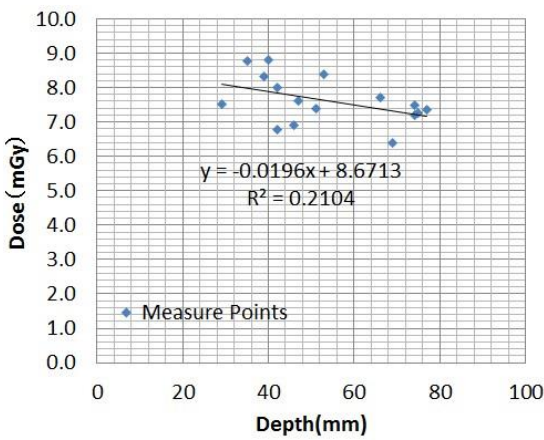
Fig. 4-8 Depth of measure points
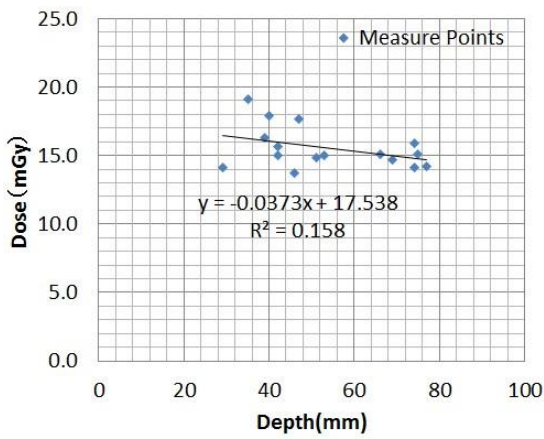
a)AEC off (Pelvis)

b)AEC off (Abdomen)

c)AEC on (Pelvis)
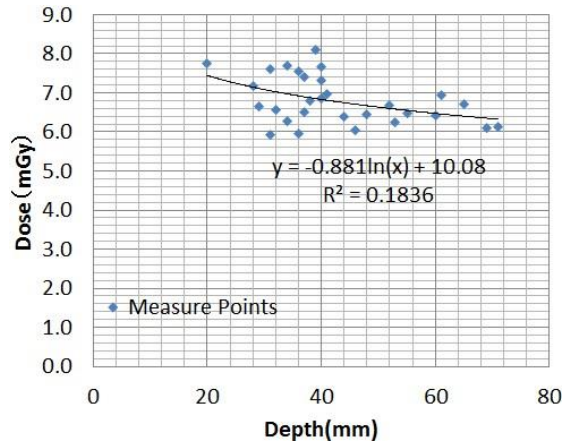
d)AEC on (Abdomen)

Fig. 4-9 The relation between depth of measure points and doses without the material

The depth of each organ was evaluated by averaging the depth of measure points (Fig. 4-10). Figure 4-11 shows the organ doses in the scan range and the organ doses in the scan without AEC are inversely proportional to the organ depth. However, in the AEC on scans, there is not a significant correlation between the organ doses and the organ depth.
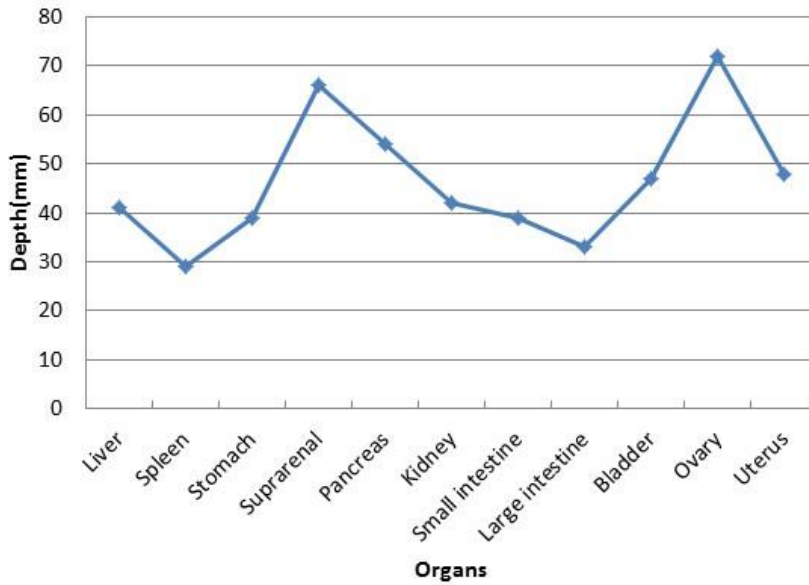
Fig. 4-10 Average depth of measure points of organs in the scan range
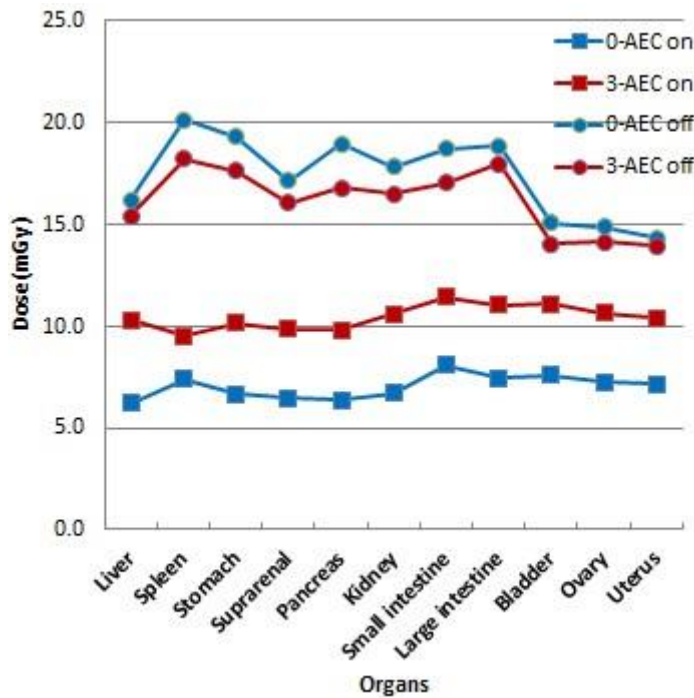
Fig. 4-11 Organ doses in the scan range

4.4 Conclusion

In this study, we described our investigation of radiation doses to overweight and obese children from diagnostic paediatric abdominal-pelvic MDCT examinations by the use of an anthropomorphic child phantom. The organ doses for the average-size child and the over-weighted child in paediatric abdominal-pelvic CT were evaluated, respectively. The effect of subcutaneous soft tissues on exposure dose was also demonstrated.

Section Ⅲ   Protection in Radiotherapy

In this section, the purpose is to test the feasibility of the prospective tracking method to predict the positions of the moving target based on the preceding position signals, and then to minimize absorb doses in normal organs surrounding targets in tumor tracking radiotherapy.

Chapter 5 The Research of Respiratory Movement Induced Hepatic Tumor Motion in Radiotherapy by Use of a Cone-beam CT under the Fluoroscopic Mode

5.1 Introduction and Objective

Radiation therapy plays an important role in the treatment of liver cancer, which is the one of the most common malignant tumors in Asia [36]. Owing to the accumulated high dose of radiation required, as well as the use of hypofractionation, attention must be paid to accuracy in treatment delivery of radiation therapy to the liver cancer. However, respiration often leads to liver movement during the therapeutic process, especially in the cranial-caudal (CC) direction, which may cause an erroneous dose [37, 38]. In order to achieve accuracy in the dose to the target, the margin extended from the clinical target volume (CTV) is ordinarily provided for three-dimensional conformal radiotherapy (3D-CRT) and intensity-modulated radiation therapy (IMRT). Furthermore, the range of the margin has a good relationship to the respiration of a patient. This could be deduced by real-time monitoring of the respiration of the patient. Maier-Hein [37] showed that mean displacement between expiration and inspiration was 15.0 ± 4.7 mm, with cranio-caudal movement making up the main part (14.2 ± 4.9 mm). In this study, we studied respiratory movement to analyze tumor motion due to respiration by use of a cone-beam CT (CBCT) installed on an Elekta Synergy-S accelerator (Fig. 5-1) under the MotionView^{TM} mode of fluoroscopy.
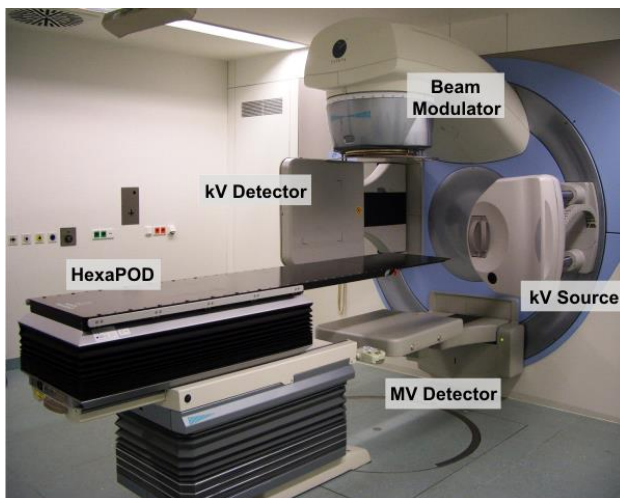
Fig. 1 An Elekta Synergy-S accelerator in treatment room

5.2 Materials and Methods

5.2.1 Materials in this study

The ventral fluoroscopic images of 5 patients with primary carcinoma of the liver were obtained with the CBCT under the MotionView^{TM} mode. All of the patients have gone through interventional therapies, and hence the concentrated lipiodol was deposited in their liver during the whole periods of radiotherapy. As the tumor marker, the movement of concentrated lipiodol could be directly observed in the images. The field range contained the movement areas of the midriff and liver. The interval between adjacent pictures was 0.183 s, and the spatial resolution was 0.5 mm.

5.2.2 Motion signal curves of midriff and tumor

The regulation of respiratory movement was studied by using the continuous fluoroscopic images which obtained during 20~40 s in each fraction. The anterior and lateral images demonstrated that the tumor movement was not obvious in the anterior-posterior (AP) and left-right (LR) directions, but was obvious in the CC direction. The lateral images were used to analyze the midriff movement because the midriff boundaries were clearer in lateral than in anterior images. A lead cross was attached on the thermoplastic immobilization as a basis point. In preparation for the irradiation, the position of the midriff and tumor relative to the lead marker should be measured according to each film of the fluoroscopic image, the reference value is the average position of the patients' midriff during respiration. The curves of movement were analyzed.

5.2.3 Movement of tumor for deep breaths and breath holding

The patients were trained to hold their breath, and the lateral fluoroscopic images were obtained. The patients were first told to breathe freely, and then, to hold their breath following directions. The relationship between midriff movement and tumor movement was studied as the patients held their breath.

5.2.4 Influence of thermoplastic immobilization on tumor movement

In order to investigate the influence of thermoplastic immobilization on respiration, the fluoroscopy was first carried out when the patients were immobilized by use of thermoplastic. Then, remove the thermoplastic immobilization and insure that patient is stable. Attached the markers to the thoracic space and abdomen of the patients, after that, the fluoroscopy was carried out again. Differences in the respiratory period and range

among the patients with and without the thermoplastic were studied, as well as the relationship between movement of skin markers and tumors.

5.2.5 Differences of tumor movement among fractions of treatment and patients

For each treatment, the lateral fluoroscopic images were obtained as the patients were calmly breathing. The movement curves for the midriff and tumor for a given patient were investigated in different fractions, and the differences of respiration among the patients were analyzed.

5.3 Results
5.3.1 Periods and ranges of the hepatic tumor movement

The movement curves of the hepatic tumor and midriff demonstrated that the range of the tumor movement was in general in accordance with the midriff movement, and the movement period was basically similar to the respiratory period. Due to the influence of the tumor position, there was a slight difference in the movement curves of the tumor and midriff. If the duration of fluoroscopy was long enough, the range of the patients' respiration would obviously fluctuate (coughing was not taken into consideration), however, the patients' respiration was relatively smooth in each fraction of the treatment (Fig. 5-2). The anterior and lateral images demonstrated that the range of tumor movement was small in the AP and LR directions. By means of investigating the range of the respiration movement in the CC direction in some continuous periods, the margin extended from CTV could be accurately planned based on the results.
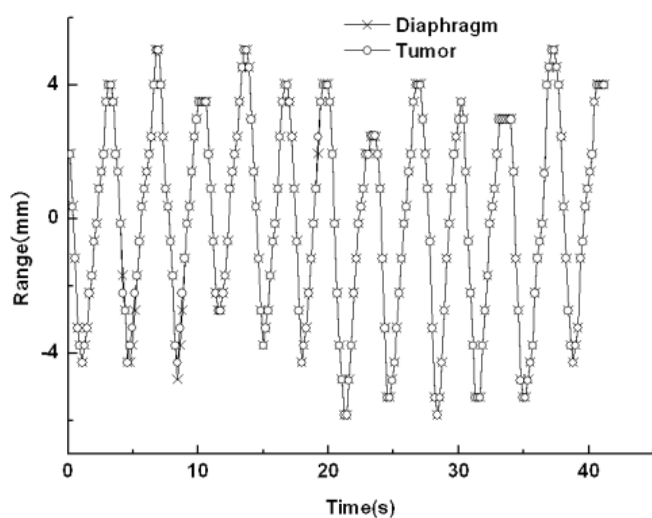

Fig. 5-2 Typical movements of tumor and diaphragm in respiration

### 5.3.2　Movement of the tumor for deep breaths and breath-holding

During the period of breath-holding after inspiration, the positions of the diaphragm and tumor almost did not change (Fig. 5-3). At the end of inspiration, the range of the tumor movement was different from the midriff movement because of the liver distortion caused by other organs, however, the period and phase stayed the same. For different patients, the breath holding time and the ranges of the midriff movement during the breath holding were different.
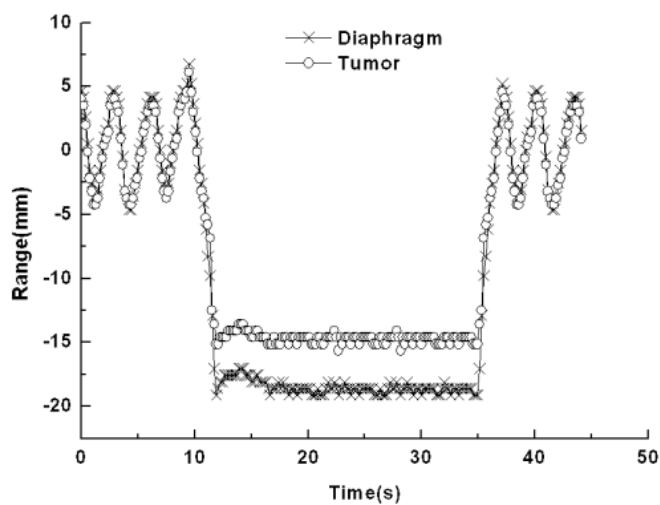
Fig. 5-3 Respiration movements for deep breathing and breath holding

5.3.3　Influence of thermoplastic immobilization on the tumor movement

Lateral fluoroscopic images were obtained with and without the thermoplastic immobilization. Furthermore, the tumor movement curves were analyzed. The results showed that the difference between the respiration periods was not obvious. However, the movement ranges were distinctly different (Fig. 5-4). Our studies demonstrated that thermoplastic immobilization of the body not only improved the positioning accuracy, but also reduced the range of tumor movement. As a result, the range of margin could be reduced in the treatment plan, so as to better to protect the normal tissue.
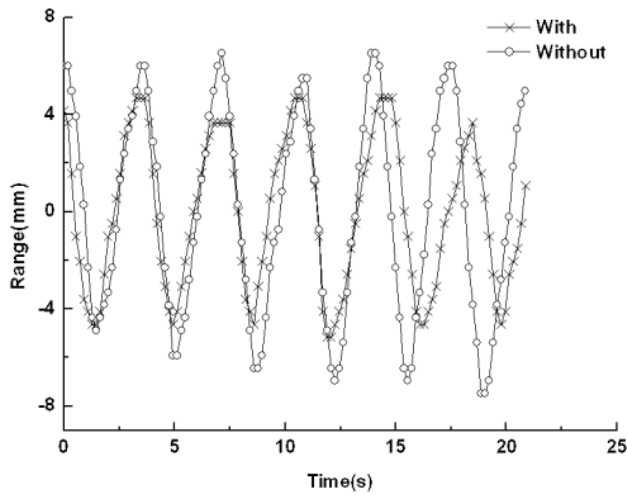
Fig. 5-4 Effect of thermoplastic immobilization on the respiration

The fluoroscopic images showed that the marker in the patient's thoracic space had no obvious motion, and the marker in the patient's abdomen moved with the respiration only in the AP direction, so that only the movement of the abdomen marker in the AP direction could be measured. As the data showed, the periods and ranges of the marker movement curves and the tumor movement curves had a good relationship (Fig. 5-5-a). We defined F1 was the marker movement curve and A1 was the average range, A2 was the average range of the tumor movement, and tried to calculate the tumor movement curve by formula F2=F1*（A2 /A1）. The result was compared with the measured tumor movement curve. The two curves were basically same, whereas the marker movement in the AP direction and the tumor movement in the CC direction differed only in the range, which showed that it was feasible to deduce the tumor movement from the marker for the tumor tracking technique (Fig. 5-5-b)
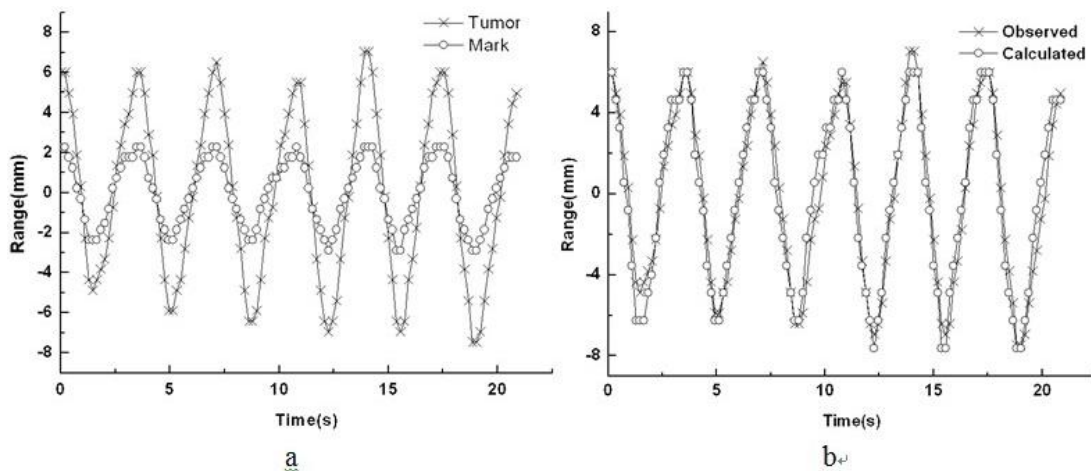

Fig. 5-5 a)Movement of tumor and skin mark during respiration; b)Measured and calculated movement curves of the skin mark

5.3.4 Differences of tumor movement among fractions of treatment and patients

Figure 5-6-a here shows the midriff movement curves in five weekly fractions. The periods of respiration for a given patient were slightly different in the five weekly fractions, and the ranges of the midriff and tumor movement caused by the respiration were almost the same. By comparing the respiration periods in fractions of the whole treatment, we found that the period of the patient's respiration was basically steady. If cough and other disturbance were not considered, the range of tumor movement was almost unchanged in the treatment.

The difference in the periods and ranges of patients' respirations were obvious (Fig.5-6-b). The respiration periods of patients were 3~4.5 s, and the range of midriff movement was 10~15 mm. For different patients, individualised treatment plan should be designed according to the respiration.
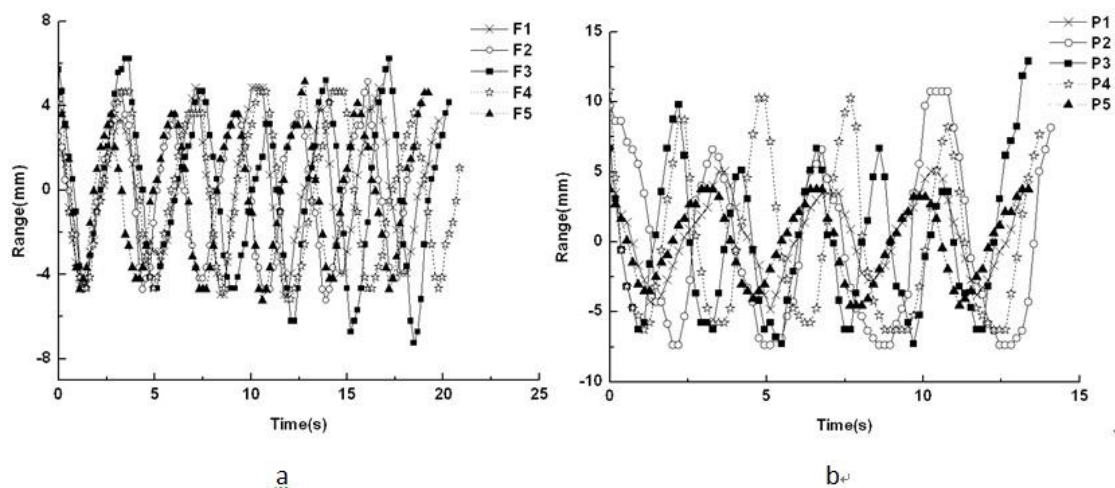
Fig. 5-6 a)Respiration movements of 5 weekly fractions; b)Five different patients' typical respiration movements

5.4 Discussion

Radiation therapy is a complex process, and many factors could influence the accurate delivery of dose to the tumor. The movements of the tumor, tissue, and organs caused by respiration had effects on the accuracy of the treatment position and dose delivered to the target volume. It would therefore, result in reduction of tumor control probability (TCP) and increase of chances of recurrence. The tumor movements of patients were obvious during radiation therapy because the liver could easily be affected by respiration. For 3D-CRT, especially for IMRT, the patients' respiration should be studied when the treatment plan is designed, selected suitable margin to ensure the

accuracy of the dose to the tumor. Our research showed that the range of movement of a liver tumor could reach 1cm in the CC direction, but was not obvious in the LR and AP directions. Due to limitation of time and space, the movement curves in the LR and AP directions could not be obtained exactly. In view of the tumor movement and the lower dose at the field border, the margin should be about 1 cm in the CC direction, as well as 5 the mm in the LR and AP directions for the treatment planning. Our results demonstrated that the period and range of respiration were stable in the whole treatment. The respiration range might be different for each patient, furthermore, the position of the tumor relative to the midriff would also determine the influence caused by tumor movement in a way, so the margin should be specially considered based on the respiration of patients for treatment planning.

Breathing control could lessen organ movement [39, 40]. As a result, the movement range of a liver tumor was lower when the patient held his breath. Multifield radiation and the normal dose-fractionated irradiation are usually used in CRT for liver cancer, and the patients should hold their breath repeatedly during the treatment. In order to fix the tumor position, the patients should have 2~3 periods of training of breath holding before they are irradiated, which makes sure that the tumor is in the irradiation area. Most patients can hold their breath for about 30 s, whereas the time of a single radiation field was about 15 s. Therefore, the tumor position was basically stable in a single radiation field. Different patients hold their breath for different times, therefore, each patient should be trained, and the regulation of tumor movement should be analyzed.

When the patient breathed freely, the tumor position could be deduced by the detectable marker attached on the patient's skin surface [41, 42]. It was worth noticing that, as the marker was put in different locations, the respiration range obtained might vary. This should be measured and analyzed according to each patient. For a given patient, the marker position should stay the same for different fractions, so as to keep the same relationship between the movement ranges of the tumor and midriff, and the formula deduced by measured data could be used repeatedly, which could reduce the burden on doctors and patients, as well as reduce the treatment time.

5.5 Conclusion

X-ray fluoroscopy can monitor the patients' tumor movement in real time, which is easy to use, costs little, and obtained reliable results. However, there must be an obvious marker such as iodinated oil, or metal marker in the patients' bodies. However, for some patients, the shape and volume of the iodinated oil might change during the whole irradiation, which has an effect on the accuracy of measurement.

Chapter 6 Feasibility Study of Predictive Tracking of Respiration Signals for Breathing Compensated in Adaptive Radiotherapy by use of Autoregressive Model

6.1 Introduction and Objective

Radiotherapy aims to precisely deliver a lethal dose to tumors while minimizing radiation dose to the surrounding healthy tissues. Since tumor movement caused by respiration usually lead to underdosage in target and overdosage in normal organs and tissues, it is a challenge for achieving this objective. A classical approach to accommodate the uncertainty of tumor location due to respiration is to add a relative large planning target volume (PTV) margin to the clinical target volume (CTV). Although this is thus irradiated to ensure adequate dose coverage of the tumor, healthy tissues complications are increased and the dose that can be delivered to a tumor is limited by the tolerance of the healthy tissues [43].

Several methods including motion-adaptive radiotherapy have been developed to increase tumor localization accuracy during irradiation, and then to ensure adequate doses in targets and minimum doses in normal organs. Breath-holding is a method to minimize the range of respiratory tumor motion [44]. Respiratory gating is proposed to reduce tumor localization errors during irradiation by limiting the radiation exposure to a portion of the breathing cycle [45]. By now, a sophisticated method is tumor tracking radiotherapy using a real-time tracking strategy to synchronize the radiation beams with the moving tumor in treatments of thoracic and abdominal tumors [46,47]. In this method, signals representing moving targets could be obtained from either real-time fluoroscopy of implanted markers near the target or other respiration sensors, a dynamic multi-leaf collimator (MLC) approach is proposed and a robotic arm is used to move the accelerator that produces the radiation beams.

However, delay time normally exists between the acquisition of motion signal and the action execution [48,49]. It was previously showed that[50] respiratory motion normally resulted in a 2 mm systematic position lag to target, with a 0.4 second delay time in general. Because of the regularity of respiratory signals can be predicted to a limited extent by using computation algorithms, this systematic lag could be compensated by predicting target movements [51-53]. The purpose of this study is to test the feasibility of the prospective tracking method to predict the positions of the moving target based

on the preceding position signals.

6.2 Materials and Methods

6.2.1 Fluoroscopy system of position measurement

For the purpose of position measurement in this study, a cone-beam CT (CBCT) attached to an Elekta Synergy-S accelerator was used under the MotionView™ fluoroscopy mode. The fluoroscopic images including the moving targets were recorded at intervals of 0.18 seconds. The motion signals were derived from the sequential fluoroscopic images.

6.2.2 Autoregressive (AR) model

The autoregressive (AR) model is one of the linear prediction formulas which attempt to predict an output yn of a system based on the previous inputs (xn, xn-1, xn-2...). The definition used here is as follows:

$$y_n = c + \sum_{i=1}^{n} a_i x_{n-i} + \varepsilon_n \, ,$$

where a_i are the parameters of the model, x_i are elements of the previous inputs, and n is the filter order, which is generally less than the number of the previous input data points; c is a constant (often omitted for simplicity) , and ε_n is white noise. An autoregressive model can thus be viewed as the output of an all-pole infinite impulse response filter whose input is white noise, and is sometimes known as a maximum-entropy model in physics applications.

Any element in a series can be evaluated by a linearly weighted sum of previous elements in the same series. The weights are the AR coefficients. The purpose of the AR analysis is to obtain the optimal values of a_i from a given previous inputs x_i. There are number of computational methods for calculating the AR coefficients. Two of the most common methods are least squares and Burg's method. In databases of MatLab, there are various preconfigured methods available for computing the AR coefficients, such as Burg's method, the covariance method (cov), and the modified covariance method (mcov). The cov and the mcov belong to the least square method. We tested Burg's method and the mcov, respectively. The dependence of the predicted errors on the model order of filter (n) and the length of the previous inputs data are also discussed in detail.

Signals of 40 data points were used, as the previous inputs, to compute the AR model coefficients. The filter order was set as half of the previous inputs length, either for Burg's method or for the mcov method. The position error of the predicted signal was computed as the average value of the absolute difference between the original signal and the predicted signal:

$$E_{predicted} = \frac{1}{N}\sum_{i=1}^{N}|y_i - x_i|, \qquad\qquad (1)$$

where N is the total number of predicted points. The position error result from time lag was calculated through shifting the original signal by two time units (~0.36 seconds), computed as the average value of the absolute difference between the original signal and the shifted signal:

$$E_{shifted} = \frac{1}{N}\sum_{i=1}^{N}|x_i - x_{i-2}|. \qquad\qquad (2)$$

6.3 Results

6.3.1　Original and predicted respiratory signals

A tumor motion signal of a volunteer patient with lung cancer was acquired by fluoroscopic images and was verified to be closely related to the free-breathing signal at that time. The anterior and lateral fluoroscopic images demonstrated that only the tumor movement in the cranial-caudal (CC) dimension was clear. Therefore, none but the motion in the CC dimension is considered and analyzed as the original signal in the study (Fig. 6-1). About 40 seconds of motion was recorded, and the whole series contains about 220 data points. The average error caused by the time lag was 1.8mm as computed by the formula (2). Figure 1 also shows the predicted signal by use of Burg's method. The number of the previous inputs was 40 and the order of filter was 20. The predicted error was nearly 0.5 mm as computed by formula (1).
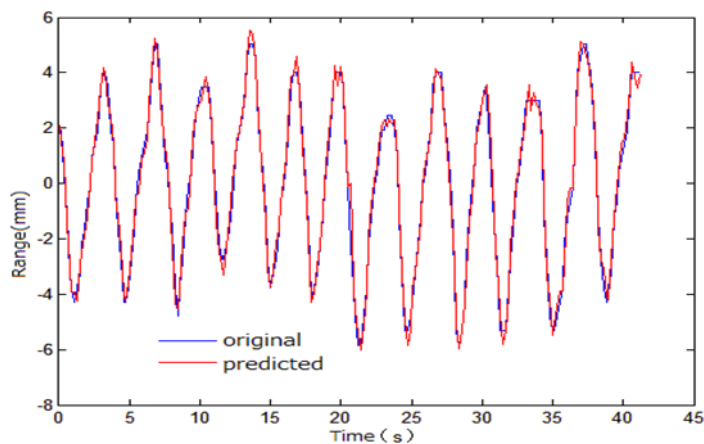
**Fig. 6-1** The predicted signal compare with the original regular signal

Moreover, a motion signal will be irregular when the target is close to the heart. Although the signal is irregular, in this study, Burg's method still has a good performance in prediction (Fig. 6-2). In this case, the average error caused by the time lag was about 2.1 mm, and the predicted error was computed to 0.4 mm.
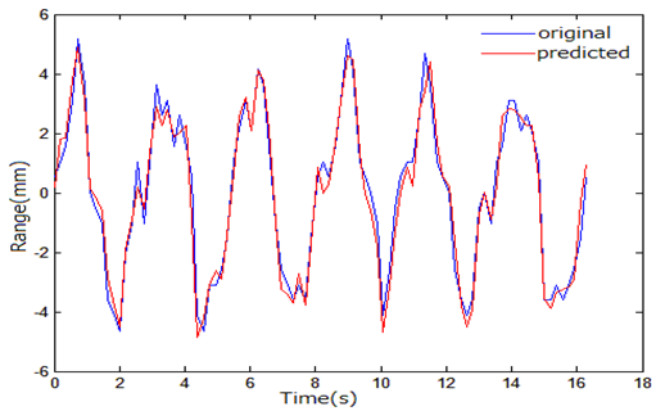
Fig. 6-2 The predicted signal compare with the original irregular signal

6.3.2　Relationship between the predicted errors and the filter orders

It is difficult to determine the most correct filter order in a straightforward way. This study shows the relationship between the predicted errors and the filter orders, when the input data length were 40, for Burg's method and the mcov method, respectively (Fig. 6-3). As the filter order increases, the average error decreases quickly but then more slowly. As the Figure 3 shows, Burg's method has a limited advantage after the filter order exceeding 10 comparing with the mcov method.
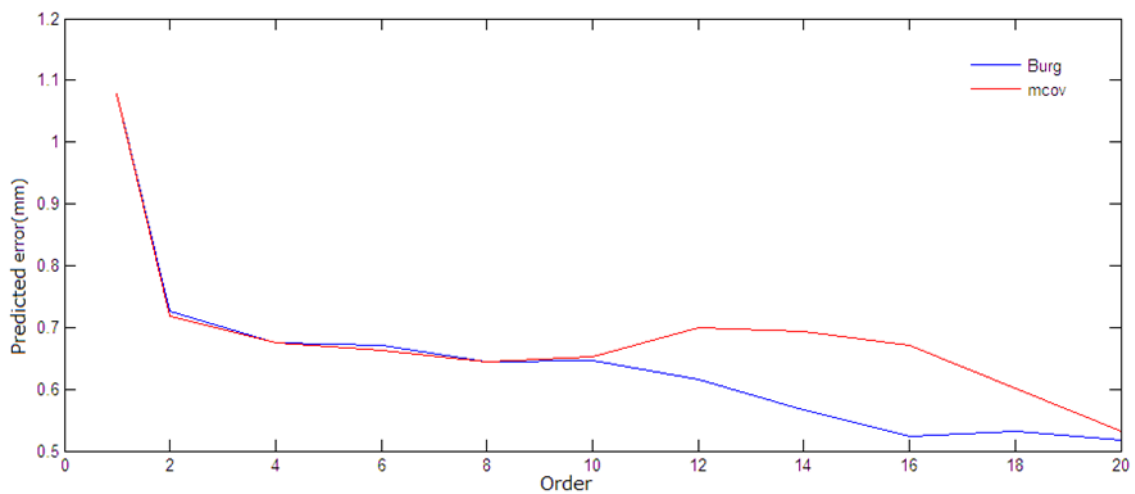
Fig. 6-3 Relationship between the predicted errors and the order of filter

66

6.3.3 Relationship between the predicted errors and the input data length

The relationship between the predicted errors and the number of the previous input data points was tested in Burg's method, by altering the length from 10 to 100 with a step of 10. The order as defined by half of the fraction of the previous input data length. The results are shown in Figure 6-4. The minimum predicted error was about 0.4 mm when the number of the previous input points was 90 and the order was 45.
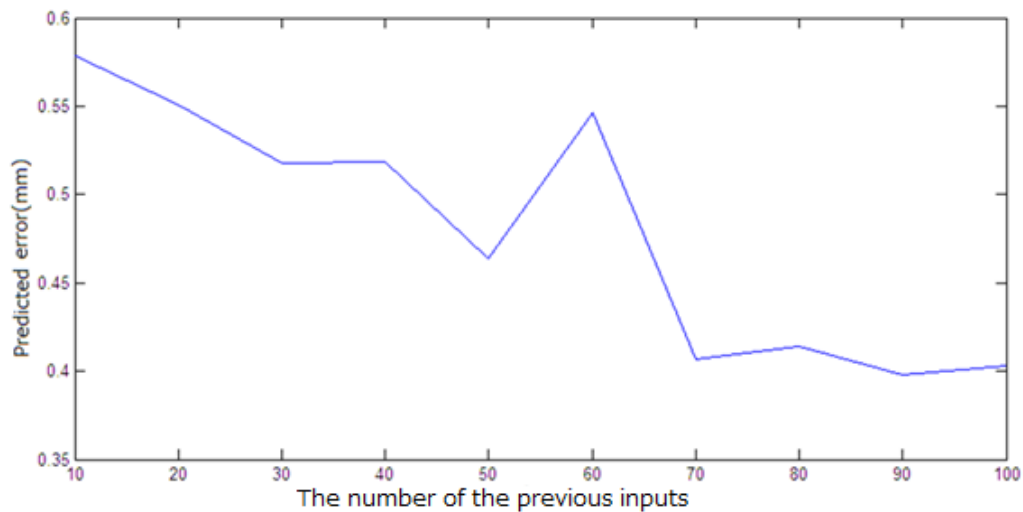
Fig. 6-4 Relationship between the predicted errors and the number of the previous inputs

6.4 Discussion

Radiation therapy uses controlled high-energy rays to treat tumors and other diseases. The goal of radiation therapy is to maximize the dose to abnormal cells while minimizing exposure to normal cells. To achieve this goal, revolutions have been realized in treatments and many advances have been made to ensure that radiation therapy is effective and safe. As one of the typical technologies, tumor tracking treatment provides practicability in both sides. The previous studies [54,55] have shown that the use of tumor tracking technology during radiotherapy treatment would result in significant reduction in dose to the healthy tissues, potentially decreasing the probability or severity of side effects. However, the time lag exists in radiation treatment system still restricts the dose optimum degree in tumor and healthy organs. Although there are so many benefits with the use of tracking technology and patients would be safer than traditional treatments, compensation for the delay time is still in need of solution.

To provide a contribution for solving this problem, the purpose of this study is to test

the feasibility of the prospective tracking method to predict the positions of the moving target based on the previous input data points. The results showed the feasibility of using AR model to predict the respiratory signals and some advantages of Burg's method comparing with the modified covariance method. In a typical case, the predicted error of free-breathing respiration signals of a volunteer patient was about 0.5 mm, while the error caused by time lag was about 1.8 mm. Moreover, the predicted error and the shifted error of the irregular signal were about 0.4 mm and 2.1 mm, respectively. The predicted error is dependent on the filter order and the length of the previous input data. Generally, the predicted error is inversely proportional to the input data length and the filter order. For this typical case, the minimum predicted error was realized as 0.4 mm when the input data was 40 points, and the filter order was half of the length.

In tumor tracking radiation therapy, high-energy photon beam is delivered under computer control during the respiratory periods. The prospective tracking system should therefore accurately predict the positions of the targets based on real-time signals. As shown in Fig.1, the present study verified the feasibility of using AR model to achieve this aim. Burg's method for AR spectral estimation is based on minimizing the forward and backward prediction errors while satisfying the Levinson-Durbin recursion. In contrast to other AR estimation methods, Burg's method avoids calculating the autocorrelation function, and instead estimates the reflection coefficients directly. The primary advantages of Burg's method are resolving closely spaced sinusoids in signals with low noise levels, and estimating short data records, in which case the AR power spectral density estimates are very close to the true values. In addition, Burg's method ensures a stable AR model and is computationally efficient. The accuracy of the Burg method is lower for high-order models, long data records, and high signal-to-noise ratios. The spectral density estimate computed by Burg's method is also susceptible to frequency shifts resulting from the initial phase of noisy sinusoidal signals. Since the data record is usually not long and then the order is low for respiratory signals in clinical treatment, it is effective to use Burg's method to predict tumor motion with the benefit of unburdened patients and low predicted errors.

Although Burg's method has been proved to be effective and advanced comparing with other AR model algorithms, additional test should be performed in the future, including the validity and efficacy of the refined prospective tracking model. Moreover, the relevance between the tumor movement and the respiratory motion should not be neglected too. Since the system is used to track and predict the signals based on respiratory motion, such as intestine tumors can't be tracked in this way.

6.5 Conclusion

In this study, Burg's method was used to predict tumor motion cause by respiratory in radiation therapy. This method has been proved to be effective to predict tumor motion in real-time, and moreover, it could make a contribution to tumor tracking technology.

Section Ⅳ　Protection in Environment

In this section, it was intended to laboratorially decontaminate the radioactive soil by use of electrokinetic remediation technology, and a new radiation shield was developed for survey meters to measure environmental radiation exposure doses accurately in badly contaminated areas in Fukushima.

Chapter 7 The Research of Decontamination of Radiocesium Contaminated Soil in Fukushima by Use of Electrokinetic Remediation Technology

## 7.1 Introduction and Objective

The Fukushima Daiichi Nuclear Power Plant (FDNPP) accident, which was caused by the catastrophic earthquake and tsunami that occurred on 11 March 2011, led to great emissions of radioactive cesium and serious soil contaminations around FDNPP and neighboring prefectures [56]. For the radiocesium ions in the contaminated agricultural soil can easily enter human bodies and make harm to people's health through the absorption of the crops, soil contaminated by radiocesium has become one of the environmental problems which should be resolved urgently in the disaster-stricken area. Electrokinetic remediation technique is a new electrochemistry remediation technology gradually developing in recent years for dealing with heavy metals, radionuclides, and organic contaminants from saturated or unsaturated soils in situ, and it is an advancing task of global environmental science and technology. Moreover, cost-effectiveness is adequate with this technology and satisfactory decontamination efficiency is expected [57,58]. In this study, it was intended to laboratorially decontaminate the radioactive soil by use of electrokinetic remediation technology, with the aim of the environmental risk reduction and the land reproduction.

7.2 Materials and Methods

7.2.1 Electrokinetic remediation technique

Electrokinetic remediation technique is a new electrochemistry remediation technology gradually developing in recent years for dealing with heavy metal contaminated soils in situ, and it is an advancing task of global environmental science and technology [59]. The general schematic of this method is similar to that of an electrolytic cell and is shown in Fig. 7-1. Generally, a low-voltage DC electric current is applied via electrodes immersed in a saturated soil results in oxidation at the anode site and the reduction at the cathodic site, generating an acid front that cause desorption and dissolution of heavy metals. Under the condition of low current density, pollutants soluble in water or adsorbed in the surface layer of the soil will move towards different electrodes according to charges what they hold, and the bonds between pollutants and

soils will be broken down with anodic acidification. Water will flow in soil in the form of electro-osmotic flow and the fluids in the micropores can be brought to the anode, so as to make the dissolved pollutants transfer to the surface layer, and thus are removed.
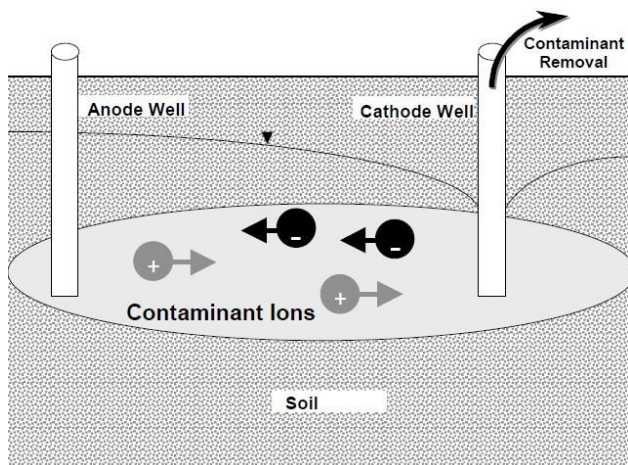
Fig. 7-1 General schematic of electrokinetic remediation

7.2.2 Materials in this study

In this study, radioactive cesium contaminated soil (Photo. 7-1) was collected from a polluted area in Fukushima and was classified by grain size to the fine soil and the rough soil. The PH value of the experimental solution was modulated by use of HASAL Liquid (Photo. 7-2). HASAL settling agent (Photo. 7-3) was used to precipitate the cesium ions in the experimental solution after decontamination. A personal NaI scintillation survey meter (Photo. 7-4) was used to monitor background doses of the experiment area. It was also used to measure the specific activity of the soil before and after decontamination with a connection to a computer, which was installed with software for displaying different isotopes of cesium directly. The PH value of the experimental solution was detected by use of a PH calibration (Photo. 7-5). A DC power supply (Photo. 7-6) kept providing direct current between the electrodes during electrokinetics.

Photo. 7-1 Radioactive cesium contaminated soil

Photo. 7-2 HASAL Liquid

Photo. 7-3 HASAL settling agent

Photo. 7-4 The personal NaI scintillation survey meter

**Photo. 7-5** The PH calibration

Photo. 7-6 The DC power supply

7.2.3 The electrokinetic remediation system

The electrokinetic remediation system used in this experimental study was composed of a buffer tank, an experiment tank and a chemical precipitation tank. The process of the electrokinetic experiment was as following: Firstly, the right amount of HASAL Liquid was mixed with the water in the buffer tank to produce acidic or alkaline solution. Then secondly, the solution was poured into the experiment tank. A certain amount of the contaminated soil was added in and the electrodes were set up. The direct current power was turned on and electrokinetics was started. Thirdly, when the remediation was finished, the solution was moved into the chemical precipitation tank. The settling agent was added to precipitate the cesium ions. At the end, the sediment and the decontaminated soil were collected and dried, the solution was also kept. To evaluate the decontamination effect of electrokinetics, the radioactivity of the soil was dried and was measured before and after the remediation, and the specific activity of the solution and the cesium precipitant was measured too.

The electrokinetic processing time was controlled to be 1 hour. The weight of the soil in each experiment was 500g. The electric voltage was supplied to be 30 volt (V). The fine soil and the rough soil were remedied respectively to evaluate the influence of the grain size of soil. To evaluate the effect of PH value of solution, acidic solution and alkaline solution was prepared for remediation respectively. Each program was repeated 3 times, and the average values were reported. The treatment process in the experiment tank and in the precipitation tank is shown in Photo. 7-7 and Photo. 7-8, respectively.
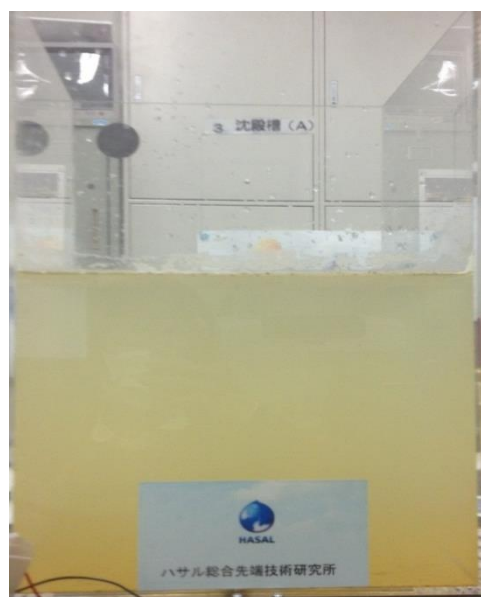
Photo. 7-7 Process in the experiment tank   **Photo. 7-8** Process in the precipitation tank

7.3 Results

7.3.1　The results of remediation for the fine soil with acidic solution

The results of remediation for the fine soil with acidic solution are shown in Table 7-1. The PH value of the solution in this treatment was controlled to be 3.75. The acid solution was assumed to be nonradioactive before the radioactive soil was add in. Specific activity of ^{137}Cs in each material was reported, and that of ^{137}Cs and ^{134}Cs was also evaluated in total. According to the results, the specific activity of ^{137}Cs in the fine soil before and after decontamination was 25700 Bq/kg and 16200 Bq/kg, respectively. The rate of decontamination was computed to be 37% by considering the value before decontamination as the reference level. The radioactivity of ^{137}Cs in the precipitate was 10900 Bq/kg because of the cesium ions in the solution was precipitated by the settling agent. Moreover, the total radioactivity of ^{137}Cs and ^{134}Cs in the soil was 40950 Bq/kg and 25400 Bq/kg before and after decontamination, and it was 16530 Bq/kg in the precipitate. The rate of decontamination was 38%, and it was almost the same as that to ^{137}Cs. The results show that electrokinetics would be effective to extract radiocesium from polluted soil, and there is nearly no difference between the rate of decontamination to ^{134}Cs and to ^{137}Cs.

	Materials	^{137}Cs (Bq/kg)	^{137}Cs + ^{134}Cs(Bq/kg)
Before decontamination	Fine soil	25700	40950
After decontamination	Fine soil	16200 (-37%)	25400 (-38%)
	Solution after electrokinetics	860	1450
	Solution after precipitation	200	280
	Precipitate	10900	16530

Table 7-1 Specific activity of cesium in each material before and after decontamination for the fine soil with acidic solution

7.3.2　The results of remediation for the rough soil with acidic solution

The results of remediation for the rough soil with acidic solution are shown in Table 7-2. The remediation for the rough soil was carried out under the same condition for the fine soil. According to the results, when the radioactivity of ^{137}Cs in the rough soil before and after decontamination was 19570 Bq/kg and 14770 Bq/kg, the rate of decontamination was reported to be only 25%. On the other side, the rate of decontamination was 29% in total. Comparing with the results for the fine soil, it could

be concluded that the effect of remediation for fine soil is better than that for rough soil by use of electrokinetics under the same condition.

	Materials	^{137}Cs (Bq/kg)	^{137}Cs $+^{134}$Cs(Bq/kg)
Before decontamination	Rough soil	19570	31400
After decontamination	Rough soil	14770 (-25%)	23300 (-26%)
	Solution after electrokinetics	720	1210
	Solution after precipitation	180	270
	Precipitate	9930	15830

Table 7-2 Specific activity of cesium in each material before and after decontamination for the rough soil with acidic solution

7.3.3   The results of remediation for the fine soil with alkaline solution

To evaluate electrokinetics with solution in different acid-base property, a remediation for the fine soil was carried out by use of alkaline solution to compare with the remediation under the previous acidic condition. The results of remediation for the fine soil with alkaline solution are shown in Table 3. When the PH value of solution was controlled to be 10.05 in this situation, the rate of remediation to ^{137}Cs increased from 37% to 46%, and that to ^{137}Cs and ^{134}Cs in total increased from 38% to 48%. The results show that alkaline solution is more effective in electrokinetic remediation comparing with the acidic solution.

	Materials	^{137}Cs (Bq/kg)	^{137}Cs $+^{134}$Cs(Bq/kg)
Before decontamination	Fine soil	25930	41400
After decontamination	Fine soil	13970 (-46%)	21600 (-48%)
	Solution after electrokinetics	1240	2000
	Solution after precipitation	190	220
	Precipitate	9700	14870

Table 7-3 Specific activity of cesium in each material before and after decontamination for the fine soil with alkaline solution

7.4 Discussion

Electrokinetics is a developing technology that is intended to separate and extract heavy metels, radionuclides, and organic contaminants from saturated or unsaturated soils, sludges and sediments, and groundwater [60]. The goal of electrokinetic remediation is to effect the migration of subsurface contaminants in an imposed electric field via electroosmosis, electromigration and/or electrophoresis. These phenomena occur when the soil is electrically charged with a low voltage current. The fundamental configuration for all three processes involves the application of an electrical potential between electrode pairs that have been implanted in the ground on each side of a contaminated soil mass. The cesium almost exists in ionic condition in soils. As the same chemical element, although ^{137}Cs and ^{134}Cs are different isotopic ions, cesium ions in electromigration would be treated through the same process. Therefore the rate of remediation to ^{137}Cs and to ^{134}Cs is not discrepant with either acidic solution or alkaline solution.

In General, electrokinetic remediation pollution extraction rate and efficiency is dependent upon many subsurface characteristics such as grain size, ionic mobility, contamination concentration, total ionic concentration, and the soil pore water current density [61]. Due to the different particle size, physical characteristics are so different that cesium solubility, soil conductivity, and electromigration rate are dissimilar. In this case, the remediation rate to the fine soil was 10% higher than that to the rough soil. According to the results, the fine soil is more easily to be remediated than the rough soil.

In the process of electromigration in electrokinetics, oxidation of water occurs at the anode and generates hydrogen (H$^+$) ions. H$^+$ ions generate an acid front, which migrates to the cathode. In contrast, reduction of water occurs at the cathode and generates hydroxyl (OH-) ions, which migrate as a base front towards the anode. The transport of the H+ ions is approximately two times faster than the OH- ions. Thus, the acid front moves at a greater rate than the base front. Unless the transport of the proton (H+ ion) is retarded by the soil buffering capacity, the soil between the electrodes will be acidified. This acidification often results in solubilization of contaminants due to desorption and dissolution of species from soil. Once contaminants are present in ionic form in the soil pore fluid, they migrate to the electrode opposite in polarity under the applied electric field and/or via electroosmosis, leading to their extraction from the soil at the electrodes [62,63]. However, since the high solubility as an alkaline metal ion, cesium ion is considered that be more easily extracted by use of alkaline water in electrokinetics. In this study, the same fine soil was decontaminated by use of acidic water and alkaline

water, respectively. The results shown that the remediation rate in alkaline water increased by 10% comparing with that in acidic water. This is a significant difference between the electrokinetic remediation for radiocesium and many heavy metals contaminated soils.

According to the results in this study, electrokinetic remediation has been proven to be effective to extract radiocesium from contaminated soils. Electrokinetics is an in situ process which can be highly targetable to the specific area to be cleaned since treatment only occurs between the electrodes. It also allows decontamination without removing contaminated soil. Its energy needs are relatively small compare to excavation. When cost-effectiveness and technical feasibility of other remedial options prohibit their use, electrokinetic remediation may offer an alternative at sites contaminated with inorganic species.

However, although electrokinetics may be utilized for site remediation under conditions which normally limit in situ approaches because of its so many advantages, the process has associated limitations [64]. The electrokinetic process is limited by the solubility of the contaminant and desorption of contaminants from the soil matrix. Acidic or alkaline conditions and electrolytic decay can corrode some anode materials. The presence of naturally occurring ions and organic material as well as organic contaminants can result in the development of potentially hazardous by-products when an electric field is applied to the soil. The addition of ions to the soil as a result of the amendment addition to the cathode well may also result in the formation of hazardous by-products during operation of the technology. Laboratory treatability testing as currently designed cannot identify the potential for byproduct production. There are more tests should be carried out until achieve the goal.

7.5 Conclusion

In this study, radiocesium contaminated soil was laboratory depolluted by use of electrokinetic remediation technology. The results of the experiments show that electrokinetcis is an effective method to extract radiocesium from soil. Although it is necessary to do more test in situ to carry out the remediation, this method would make a contribution to remedy contaminated soil in Fukushima.

Chapter 8 Development and research of the EARTHSHIELD — a radiation shield used for environmental radiation exposure measurement in the Fukushima nuclear accident

8.1 Introduction and Objective

In the Eastern Japan earthquake disaster 2011, radioisotopes that leaked from the Fukushima Daiichi nuclear power plant accident caused notable radioactive contamination in forests and farmland [65]. In order to evaluate the radiation intensity in the living environment, an effective dose rate is usually measured in the unit of μSv/h and is becoming one of the environmental management indicators.

An environmental radiation exposure measurement is also often carried out by a personal NaI scintillation survey meter and a GM pipe-type survey meter, besides use of a radiation monitoring post that is a small building fitted with electronic equipment to monitor radiation levels in the air [66]. Moreover, before and after decontamination work, measurements with use of survey meters are usually carried out for confirmation of the decontamination effects [67]. However, in an area having a high radiation dose, survey meters will detect gamma radiation from other contaminated areas surrounding the depolluted region, and then cannot precisely measure the radiation dose after the decontamination work.

To solve this problem, we developed a radiation shield (called EARTHSHIELD as following) for survey meters to measure environmental radiation exposure doses accurately in badly contaminated areas [68]. EARTHSHIELD is made of the Pb-based material that is more than 90% of purity in lead. It is composed of a main shield, a probe shield, and a tray. For accurate measurement of ground surface radiation doses after depollution operations, the structure and the combination of the three parts of the EARTHSHIELD are discussed in detail.

8.2 Materials and Methods

8.2.1 Study about the thickness of the main shield

The shielding effect of the EARTHSHIELD is largely dependent on the thickness of the Pb-based materials. To decide the thickness of the main shield, dose attenuation rates of the materials in a series of thicknesses were measured. A Hitachi-Aloka TCS-151 survey meter was used for measurements with a standard ^{137}Cs-sealed radioactive source. The survey meter was in a location where the radiation dose rate in the air was adjusted to the reference level of the 10.00 μSv/h and the count was 45 cps at the position. The effective dose rates and the counts were measured when a series of lead plates were inserted between the source and the survey meter, and then the attenuation rates were calculated based on the effective dose rates and the counts, respectively. The lead plates were made of the same materials as the EARTHSHIELD. The thickness of the plate was increased from 0.3 mm to 30.0 mm step by step. The measurement is shown in Figure 8-1. The thickness of the main shield was decided according to the results of the measurements.

Fig. 8-1 The measurement of the attenuation rate of the lead plate in the radiation controlled area is shown. The survey meter was set up at the position where the radiation dose rate was 10.00 μSv/h and the count value was 45 cps. The lead blocks were used to reduce the effect of the scattered rays. The lead plate was inserted between the source and the survey meter. The thickness of the plate was increased from 0.3 mm to 30 mm. The radiation dose rate and the count with the each thickness of the plate were recorded and were used to calculate the each attenuation rate.

8.2.2 Study about the height of the probe shield

In many cases, an environmental radiation exposure measurement is possibly carried out without the main shield but with the probe shield only. In this situation, the probe shield should be high enough to limit the radiation rays that would be detected through the upper opening of the shield. To decide the height of the probe shield of the EARTHSHIELD, we measured the attenuation rates of the probe shields in a series of

heights. All of the probe shields were 2cm in thickness, and the height of the probe shield was increased from 3 cm to 12 cm. The measurements were carried out in a radiation controlled area with a standard ^{137}Cs-sealed radioactive source and in an outdoor environment at Kooriyama City, Fukushima. The 3-cm-height probe shield is shown in Figure 8-2, the measurement in the radiation controlled area is shown in Figure 8-3, and the measurement at Kooriyama City is shown in Figure 8-4.

Fig. 8-2 The 3-cm-height probe shield is shown.

Fig. 8-3 The measurement of the attenuation rate of the probe shield in the radiation controlled area is shown. The probe of the survey meter was set up at the position where the radiation dose rate was 21.30 µSv/h. The probe was inserted into the probe shield, and then the radiation dose rate was recorded. The height of the probe shield was increase from 3 cm to 12 cm. The attenuation rate of the each probe shield was calculated.

Fig. 8-4 The measurement of the attenuation rate of the probe shield at Kooriyama City is shown.

8.2.3   Shielding effect of the EARTHSHIELD

There are three parts in a complete set of the EARTHSHIELD. Moreover, the different combination of the three parts should be used under the different requirement. To evaluate the shielding effect of the different combination, we measured radiation dose rates, and then calculated the attenuation rate of the each combination. The distance between the source and the survey meter was increased from 5 cm to 30 cm in the measurement. The effective dose rate was measured with no use of any shield and was regarded as the reference for the calculation of the attenuation rate at the each position. The combination of the probe shield and the main shield is shown in Figure 8-5.

Fig. 8-5 The combination of the probe shield and the main shield is shown. The probe shield was attached to the main shield, and the probe of the survey meter was inserted into the probe shield.

8.3 Results and Discussion

8.3.1 The attenuation rates with different thicknesses of the lead plates

The results of the attenuation rates with different thicknesses of the lead plates are shown in Fig. 8-6. The horizontal axis shows the thickness of the plate from 0 mm to 30 mm, and the vertical axis shows the calculated attenuation rates based on the μSv/h level and the cps level. According to the results, the attenuation rate improved with the increase of the thickness of the plate, and it became less than 10% when the thickness of the plate exceeded 20 mm. Since the attenuation rates were measured with a standard ^{137}Cs-sealed radioactive source, the results were regarded to be available in the present decontamination work places. Therefore, we decided the thickness of the main shield of the EARTHSHIELD to the 30 mm after considering the balance among the shielding effect, manufacturing cost, and the practicability.
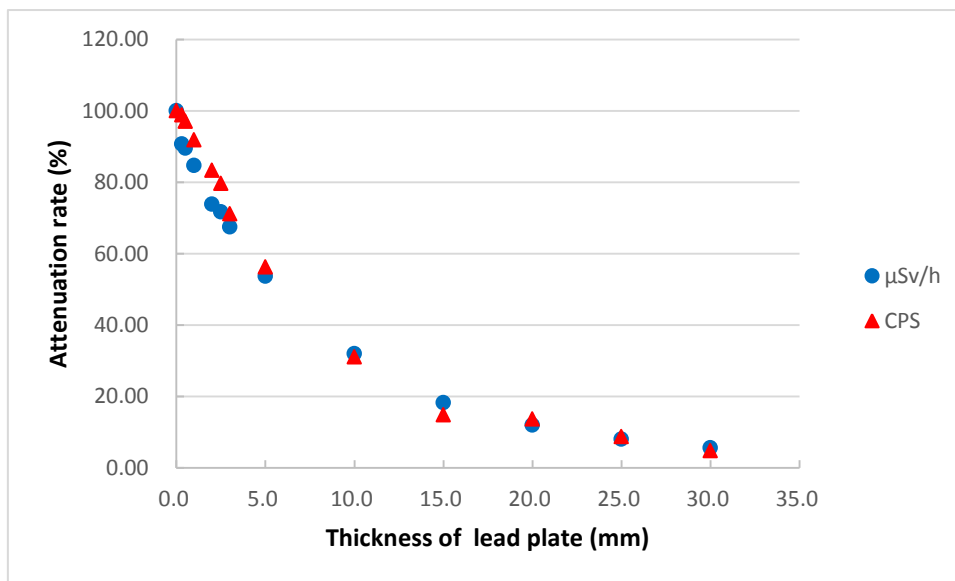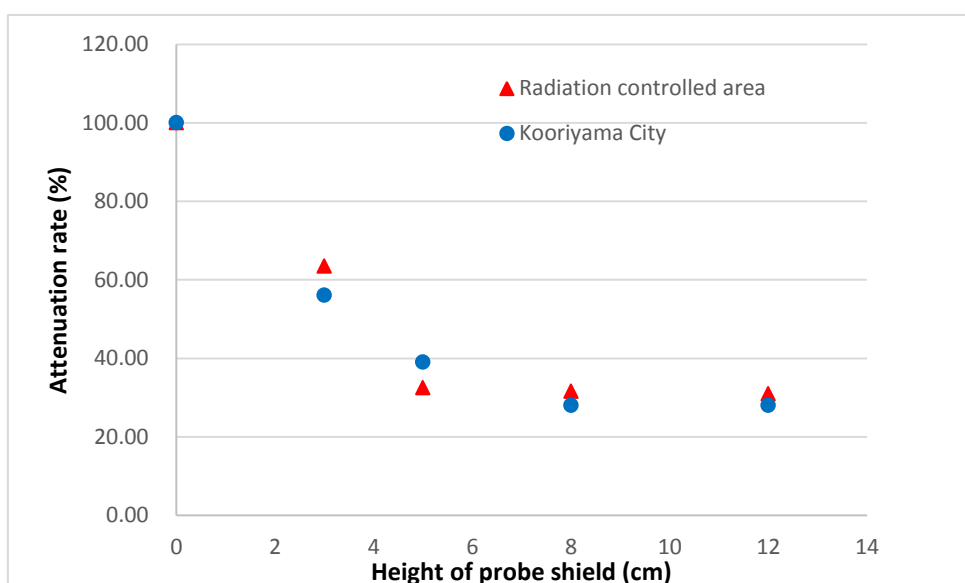

Fig. 8-6 Attenuation rates with different thicknesses of the lead plates

8.3.2 The attenuation rates with the different heights of the probe shields

The results of the study about the attenuation rates with the different heights of the probe shields are shown in Fig. 8-7. The horizontal axis is the height of the probe shield, and the vertical axis is the attenuation rate. According to the results, the attenuation rate improved with the increase of the height of the probe shield. However, while the radiation dose rate in the air had a 21.30 μSv/h level in the controlled area, the attenuation rate was only 31% although the height of the probe shield was increased to

12 cm. In addition, the attenuation rate decreased hardly even if the height of the probe shield was increased from 8 cm to 12 cm. We suggested that was because of the probe shields were only 2 cm in thickness and could be easily penetrated by radiation rays. The environmental radiation dose rate in Kooriyama City was 0.82 μSv/h, and the attenuation rate was still higher than 30% even if the probe shield was higher than 8 cm. According to the results, we suggest that the height of the probe shield should be no less than 8 cm to be used effectively for the environmental radiation measurement. Moreover, it is necessary to choose a suitable height for the probe shield, according to the survey meter which is used for measurements.
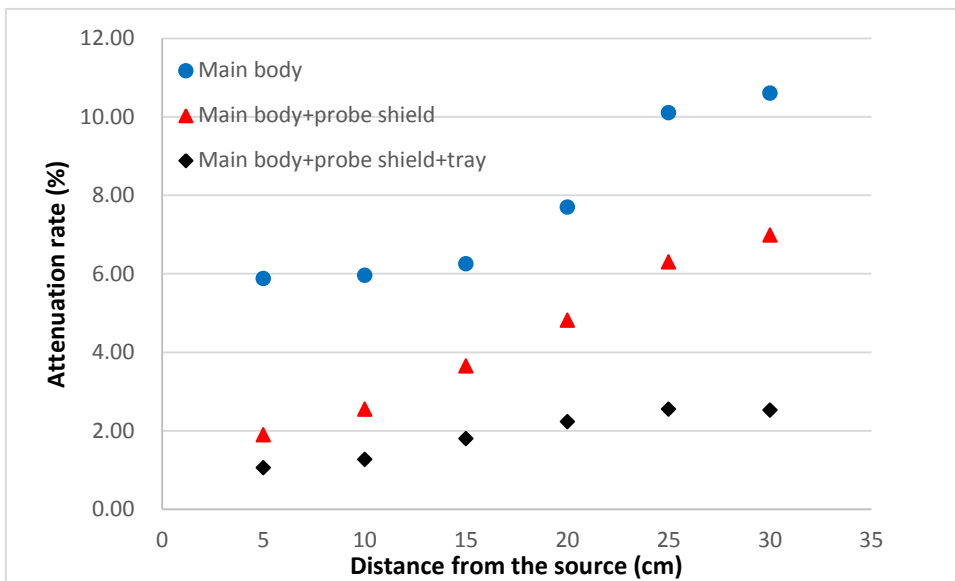

Fig. 8-7 Attenuation rates with different heights of the probe shields

8.3.3 The attenuation rates for the different combinations of the three parts of the EARTHSHIELD

The attenuation rates for the different combinations of the three parts of the EARTHSHIELD are shown in Fig. 8-8. The attenuation rates for the different combinations were measured and calculated at the each position where the survey meter was. The distance between the survey meter and the source is shown in the horizontal axis; the effective dose rate decreased from the 5.10 μSv/h at the distance of 5 cm to the 0.83 μSv/h at the distance of 30 cm. The vertical axis shows the attenuation rates for the different combinations. While the attenuation rate was 6% with only use of the main shield at the distance of 5 cm, it was improved to 2% with use of the combination of the main shield and the probe shield. Moreover, the attenuation rates got slightly worse when the distance from the source was increased. We considered that this was caused by

the fact that the gamma radiation scattered from the walls of the controlled area became easier to be detect through the upper opening of the main shield. However, according to the results, the combination of the main shield and the probe shield has an attenuation rate that is lower than 7%, and then it is enough to evaluate decontamination work effects effectively. To deal with the radiation that would be detected through the upper opening, we suggest that it would be better to add a cover shield upon the main shield.

Fig. 8-8 Attenuation rates for the different combinations of the three parts of the EARTHSHIELD

8.4 Conclusion

In this study, we measured attenuation rates by use of a dose survey meter to develop a survey meter shield for precise measurements of the environmental radiation that changed greatly after the Fukushima accident. We evaluated the shielding effect of the main shield and the probe shield of the EARTHSHIELD, aimed to measure precisely the ground surface radiation dose after decontamination work. Eventually, The EARTHSHIELD for dose survey meters was developed to measure the environmental radiation dose actually after the Fukushima nuclear power plant accident. The radiation dose of the ground surface became precisely measurable by use of the EARTHSHIELD before and after decontamination work. EARTHSHIELD will make a contribution to the precise evaluation of decontamination work.

Chapter 9   Summary

With the continuous developments of radiation science, radiation and nuclear technology is increasingly applied in many areas of modern life. Applications of radiation and nuclear technology bring many benefits but also with a lot of potential hazards for the living and natural environment. Since ionization can cause damage within a cell, which could eventually lead to cancer, a mutation in genetic material, or more immediate types of physical harm to humans, we need to be careful around radiation and pay enough attention to radiation protection.

When handled correctly, radioactive materials have many beneficial uses; misused, however, it can pose a significant danger. For examples, some patients suffered from phalacrosis, damage of skin and even cancer cause of overdosage; Secondary tumors have been diagnosed because the doses in organs surrounding the targets were too high in radiation therapy; Leakage of radioactive materials would severely affect the ecological environment in surrounding areas.

In this study, it was intended to meet the requirements with the center of radiation protection dose in a wide range which attracts the most attention and are involved, either directly or indirectly, with ionizing radiation, including diagnostic exposure doses in paediatric CT, radiation doses in normal tissues which surrounding the targets in radiotherapy, and environmental exposure doses in Fukushima nuclear accidental areas.

The reference radiation dose and organ doses from chest CT studies of children were estimated by using the data of clinical practice of the National Center for Child Health and Development in Japan. Compare with previous studies, this review shows lower exposure dose of chest CT scan in Japan, with a scan protocol system uses a color assignment based on the length or weight of a child. We described our investigation of radiation doses to overweight and obese children from diagnostic paediatric abdominal-pelvic MDCT examinations by the use of an anthropomorphic child phantom. The organ doses for the average-size child and the over-weighted child in paediatric abdominal-pelvic CT were evaluated, respectively. The effect of subcutaneous soft tissues on exposure dose was also demonstrated.

To provide a method for predicting the positions of the moving targets based on the preceding position signals, tumor motion signals were measured and analyzed by use of a CBCT installed on an Elekta Synergy-S accelerator under the MotionView^{TM} mode of fluoroscopy. The results demonstrated that movements of thoracic and abdominal tumors have a good relation to patient's respiration in the CC direction. Burg's Method

was used to predict tumor motion cause by respiratory. This method has been proved to be effective to predict tumor motion in real-time, and moreover, it could make a contribution to tumor tracking technology.

The Fukushima Daiichi Nuclear Power Plant accident, which was caused by the catastrophic earthquake and tsunami that occurred on 11 March 2011, led to great emissions of radioactive cesium and serious soil contaminations around FDNPP and neighboring prefectures. Radiocesium contaminated soil was laboratory depolluted by use of electrokinetic remediation technology. The results of the experiments show that electrokinetcis is an effective method to extract radiocesium from soil. Although it is necessary to do more test in situ to carry out the remediation, this method would make a contribution to remedy contaminated soil in Fukushima. To precisely measure radiation dose after decontamination work, a new radiation shield was successfully developed for survey meters to measure environmental radiation exposure doses accurately in badly contaminated areas.

Acknowledgements

Hopefully, readers would find this thesis somewhat useful. And I also appreciate suggestions and comments that will contribute to the improvement of my thesis.

References

1. Radiation Protection Regulations.
   http://laws-lois.justice.gc.ca/eng/regulations/SOR-2000-203/.
2. UNSCEAR 2000 REPORT.
   http://www.unscear.org/unscear/publications/2000_1.html.
3. ICRP Publication 60. Recommendations of the International Commission on Radiatiological Protection. Annal of the ICRP 21, 1990.
4. Introduction to Radiation. Minister of Public Works and Government Services Canada (PWGSC). CC172-93/2012E-PDF.　ISBN 978-1-100-21572-3, 2012.
5. Introduction to Radiation Protection.
   http://science-stories.org/stories/Radiation%20Protection.pdf.
6. Kaushik A, Mondal A, Dwarakanath BS, et al. Radiation Protection Manual. A publication of Institute of Nuclear Medicine and Allied Science (INMAS), DRDO, Delhi, India, 2010.
7. Watson DJ and Coakley KS. Paediatric CT reference doses based on weight and CT dosimetry phantom size: local experience using a 64-slice CT scanner. Pediatr. Radiol. 40:693-703, 2010.
8. Shrimpton PC, Hillier MC, Lewis MA, et al. National survey of doses from CT in the UK: 2003. Br. J. Radiol. 79:968-980, 2006.
9. Kubo T, Lin PJP, Stiller W, et al. Radiation dose reduction in chest CT: A review. AJR. 190:335-343, 2008.
10. Lucaya J, Piqueras J, García-Peña P, et al. Low-dose high-resolution CT of the chest in children and young adults: dose, cooperation, artifact incidence, and image quality. AJR. 175:985-992, 2000.
11. Mettler FA Jr, Wiest PW, Locken JA, et al. CT scanning: patterns of use and dose. J. Radiol. Prot. 20:3533-3559, 2000.
12. Hart D and Wall BF. UK population dose from medical X-ray examinations. Eur. J. Radiol. 50:285-291, 2004.
13. FDA Public Health Notification. Reducing Radiation Risk from Computed Tomography for Pediatric and Small Adult Patients. 2001, at http://www.fda.gov/cdrh/safety/110201-ct.html
14. Brenner DJ, Elliston CD, Hall EJ, et al. Estimated risks of radiation-induced fatal cancer from pediatric CT. AJR. 176:289-296, 2001.
15. Fujii K, Akahane K, Miyazaki O, et al. Evaluation of organ doses in CT examinations with an infant anthropomorphic phantom. Radiat. Prot. Dosim. pp.1-5,

2011.

16. Frush DP, Soden B, Frush KS, et al. Improved pediatric multidetector body CT using a size-based color-coded format. AJR. 18:721-726, 2002.

17. Singh S, Kalra M, Moore MA, et al. Dose reduction and compliance with pediatric CT protocols adapted to patient size, clinical indication, and number of prior studies. Radiology. 252:200-208, 2009.

18. Miyazaki O, Horiuchi T, Masaki H, et al. Estimation of adaptive computed tomography dose index based on body weight in pediatric patients. Radiat. Med. 26:98-103, 2008.

19. Ait-Ali L, Andreassi MG, Foffa I, et al. Cumulative patient effective dose and acute radiation-induced chromosomal DNA damage in children with congenital heart disease. Heart. 96:269-274, 2010.

20. Stamm G, and Nagel HD. CT-expo—a novel program for dose evaluation in CT. Rofo. 174:1570-6, 2002.

21. Fujii K, Aoyama T, Yamauchi-Kawaura C, et al. Radiation dose evaluation in 64-slice CT examinations with adult and paediatric anthropomorphic phantoms. Br. J. Radiol. 82:1010-1018, 2009.

22. Huang B, Law MW, Mak HK, et al. pediatric 64-MDCT coronary angiography with ECG-modulated tube current: Radiation dose and cancer risk. Am. J. Roentgenol. 193:539-544, 2009.

23. Strange GR, ed. APLS: the pediatric emergency medicine course, 3rd ed. Elk Grove: American Academy of Pediatrics and American College of Emergency Physicians, 213-214, 1998.

24. Luten RC, Wears RL, Broselow J, et al. Length-based endotracheal tube and emergency equipment in pediatrics. Ann Emerg Med; 21:900-904, 1992.

25. Huda W and Vance A. Patient Radiation Doses from Adult and Pediatric CT. AJR. 188:540-546, 2006.

26. Slovis TL. The ALARA Concept in Pediatric CT: Myth or Reality? Radiol. 223:5-6, 2002.

27. Boone JM, Geraghty EM, Seibert JA, et al. Dose Reduction in Pediatric CT: A Rational Approach. Radiol. 228:352-360, 2003.

28. Prokop M. New challenges in MDCT. Eur Radiol Suppl. 15:E35-E45, 2005.

29. Kalra MK, Saini S and Rubin GD. NY: Springer, 2008.

30. Zhang Y, Li X, Segars WP, et al. Organ doses, effective doses, and risk indices in adult CT: comparison of four types of reference phantoms across different examination protocols. Med Phys. 39(6):3404-23, 2012.

31. Isamberta A, Bonniauda G, Laviellea F, et al. A phantom study of the accuracy of CT MR and PET image registrations with a block matching-based algorithm. Cancer. 12:800-808, 2008.

32. Schindera ST, Nelson RC, Lee ER, et al. Abdominal Multislice CT for Obese Patiens: Effect on Image Quality and Radiation Dose in a Phantom Study. Acad Radiol. 14:486-494, 2007.

33. Lee C, Lee C, Lodwick D, et al. Effect of Subcutaneous Fat On Abdominal CT Dosimetry: Monte Carlo Study. Med Phys. 34:2349, 2007.

34. Schindera ST, Nelson RC, Toth TL, et al. Effect of Patient Size on Radiation Dose for Abdominal MDCT with Automatic Tube Current Modulation: Phantom Study. AJR. 190:W100-W105, 2008.

35. GE Healthcare. Tip Training in Partnership. http://www3.gehealthcare.co.uk/en-GB/Education/Offering_by_Product/~/media/Downloads/us/Education/Product-Education-Clinical/TiP-App-Library/GEHealthcare-Education-TiP-App-Library_CT-AutomA-SmartmA-Theory.pdf.

36. Yu JM, Li BS and Yan J. Radiotherapy of primary hepatocellular carcinoma. World Chinese Journal of Digestology. 17(10):1005-1007, 2009.

37. Maier-Hein L, Painka F, Muller SA, et al. Respiratory liver motion simulator for validating image-guided systems ex-vivo. Int J CARS , 2:287–292, 2008.

38. Nakamoto M, Hirayama H, Sato Y, et al. Recovery of respiratory motion and deformation of the liver using laparoscopic freehand 3D ultrasound system. Med Imag Anal,11: 429–442, 2007.

39. Yoshitake T, Shioyama Y, Nakamura K, et al. A clinical evaluation of visual feedback-guided breath-hold reproducibility of tumor location. Phys Med Biol,54(23):7171-7182, 2009.

40. Partridge M, Tree A, Brock J, et al. Improvement in tumour control probability with active breathing control and dose escalation: A modelling study. Radiot Oncol ,91(3):325-329, 2009.

41. Szegedi M, Rassiah-Szegedi P and Fullerton G. Characterization of liver motion based on implanted markers. Med Phys ,36(6):2506-2506, 2009.

42. Beddar AS, Kainz K, Briere TM, et al. Correlation between internal fiducial tumor motion and external marker motion for liver tumors imaged with 4D-CT. Int J Radiat Oncol Biol Phys,67(2):630–638, 2007.

43. Baskar R, Lee KA, Yeo R, et al. Cancer and radiantion therapy: Current advances and Future Directions. Int J Med Sci, 9:193-199, 2012.

44. Jiang SB, Wolfgang J, Mageras GS. Quality assurance challenges for

motion-adaptive radiation therapy: gating, breath holding, and four-dimensional computed tomography. Int J Radiat Oncol Biol Phys, 71: S103-7, 2008.

45. Saw CB, Brandner E, Selvaraj R, et al. A review on the clinical implementation of respiratory-gated radiation therapy. Biomed Imaging Interv J, 3:e40, 2007.

46. Nuyttens JJ, Prévost JB, Praag J, et al. Lung tumor tracking during stereotactic radiotherapy treatment with the CyberKnife: Marker placement and early results. Acta Oncol, 45: 961-5, 2006.

47. Sofie C, Marianne F, Af Rosenschöld PM, et al. Tumor-tracking radiotherapy of moving targets; verification using 3D polymer gel, 2D ion-chamber array and biplanar diode array. J. Phys: Conf Ser. 250:012051, 2010.

48. Sharp GC, Jiang SB, Shimizu S, et al. Prediction of respiratory tumour motion for real-time image-guided radiotherapy. Phys Med Biol, 49:425, 2004.

49. Ahn S, Yi B, Suh Y, et al. A feasibility study on the prediction of tumour location in the lung from skin motion. British Journal of Radiology, 77:588-596, 2004.

50. Keall PJ, Kini VR, Vedam SS, et al. Motion adaptive x-ray therapy: A feasibility study. Phys Med Biol, 46,pp:1-10, 2001.

51. Ichiji K, Homma N, Sakai M, et al. Respiratory motion prediction for tumor following radiotherapy by using time-variant seasonal autoregressive techniques. Conf Proc IEEE Eng Med Biol Soc. 6028-31, 2012.

52. Cho B, Poulsen PR and Keall PJ. Real-time tumor tracking using sequential kV imaging combined with respiratory monitoring: a general framework applicable to commonly used IGRT systems. Phys Med Biol, 55:3299, 2010.

53. Schweikard A, Glosser G, Bodduluri M, et al. Robotic motion compensation for respiratory movement during radiosurgery. Comput Aided Surg, 5, pp:263-277, 2000.

54. Cerviño LI, Jiang D and Jiang SB. MRI-guided tumor tracking in lung cancer radiotherapy. Phys Med Biol, 56:3773, 2011.

55. Harada T, Shirato H, Ogura S, et al. Real-Time Tumor-Tracking Radiation Therapy for Lung Carcinoma by the Aid of Insertion of a Gold Marker Using Bronchofiberscopy. Cancer, 95:1720-1726, 2002.

56. Qin HB, Yokoyama Y, Fan QH, et al. Investigation of cesium adsorption on soil and sediment samples from Fukushima Prefecture by sequential extraction and EXAFS technique. Geochemical Journal, 46, 297-302, 2012.

57. Huang DQ, Xu Q, Cheng JJ, et al. Electrokinetic remediation and its combined technologies for removal of organic pollutants from contaminated soils. Int. J. Electrochem. Sci., 7, 4528 – 4544, 2012.

58. In-situ electrokinetic remediation of metal contaminated soils technology status report. US Army Environmeantal Center. Report number: SFIM-AEC-ET-CR-99022, 2000.

59. Van Cauwenberghe L. Electrokinetics. Ground-Water Remediation Technologies Analysis Center. Technology Overview Report, TO-97-03, 1997.

60. Acar YB, Gale RJ, Alshawabkeh AN, et al. Electrokinetic remediation: Basics and technology status. Journal of Hazardous Materials. 40, 117-137, 1995.

61. McKinley JD, Savvidou C. numerical modeling of the electrokinetic remediation of heavy metal contaminated soil. CUED / D - SOILS / TR.292, 1997.

62. Kim SH, Han HY, Lee YJ, et al. Effect of electrokinetic remediation on indigenous microbial activity and community within diesel contaminated soil. Sci Total Environ. 408, 3162-8, 2010.

63. Hu HT. Influence of Complex on Electrokinetic Remediation of Zinc Contaminated Soil. E-Product E-Service and E-Entertainment (ICEEE) International Conference, 2010.

64. Wada S, Nakagawa K. Electrokinetic Remediation. Its Potential and Limit. Tsuchi to kiso. 50, 13-15, 2002.

65. Fukushima Nuclear Power Plant Accident. In: the International Commission on Radiological Protection. 2011. http://www.icrp.org/docs/fukushima%20nuclear%20power%20plant%20accident.pdf. Accessed 21 March 2011.

66. Kobayashi H, Sakamaki T and Masui K. Environmental Radiation Measuring Equipment. FUJI ELECTRIC REVIEW. 50(4):114-117, 2004.

67. Kakamu T, Kanda H, Tsuji M, et al. Differences in rates of decrease of environmental radiation dose rates by ground surface property in Fukushima City after the Fukushima Daiichi Nuclear Power Plant Accident. Health Phys. 104(1):102-107, 2013.

68. Quapp WJ, Miller WH, Taylor J, et al. DUCRETE: A Cost Effective Radiation Shielding Material. Spectrum, Sept 24-28, 2000.